Epidote dissolution–precipitation during viscous granular flow: a micro-chemical and isotope study

Veronica Peverelli[1], Alfons Berger[1], Martin Wille[1], Thomas Pettke[1], Pierre Lanari[1], Igor M. Villa[1,2], Marco Herwegh[1]

[1]Department of Geological Sciences, University of Bern, Bern, 3012, Switzerland
[2]Dipartimento di Scienze dell'Ambiente e della Terra, University of Milano-Bicocca, Milan, 20126, Italy

Correspondence to: Veronica Peverelli (veronica.peverelli@geo.unibe.ch)

Abstract. Deformation of polymineralic aggregates can be accommodated by viscous granular flow, a process mediated by the interplay among intracrystalline plasticity and dissolution–precipitation, each active in specific minerals at given P–T conditions. ~~Common~~Some rock-forming minerals like quartz~~,~~ and feldspars ~~and sheet silicates~~ have been intensively studied in terms of deformation processes. Instead, the deformation behavior of epidote and its role during viscous granular flow is not well investigated, although this mineral is ubiquitous in granitic rocks deforming at greenschist-facies conditions. In this contribution, we provide microstructural and geochemical evidence for the occurrence of dissolution–precipitation of epidote during deformation of an epidote-quartz vein. The main part of the vein is deformed producing a fold, which is visible due to relicts of primary-growth layering inside the vein. The deformation mechanisms active during deformation include dynamic recrystallization of quartz by subgrain rotation recrystallization, producing grain-size reduction of the primary vein quartz. ~~This~~Recrystallization occurs contemporaneously with dissolution and (re)precipitation of epidote, and grain-boundary sliding, leading to a combined process described as viscous granular flow. The combination of ~~intracrystalline plasticity,~~ grain boundary sliding and dissolution locally and repeatedly ~~produce~~produces creep cavities. These represent not only loci for nucleation of new epidote grains at the expenses of dissolved ~~one~~ones, but they also allow fluid-mediated transport of elements. The same trace element patterns between old epidote relicts and newly formed grains, with much narrower variability, indicate a process of chemical homogenization. The nature of the fluid mediating deformation is investigated using Pb–Sr isotope data of epidote, which suggest that deformation is assisted by internally recycled fluids with the addition of a syn-kinematic external fluid component.

1 Introduction

30 Deformation microstructures preserved in rocks are the result of the interplay of multiple microscale deformational processes, which may be identified and appreciated through careful petrographic studies (e.g., Passchier, 2005). These processes – which may be coupled to metamorphic reactions and diffusion (e.g., Pearce et al., 2013; Wintsch and Yeh, 2013; Bukovská et al., 2016; Giuntoli et al., 2018; Lanari and Duesterhoeft, 2019) – are the response of the grains to varying physico-chemical conditions in order to minimize the system's internal energy (e.g., Evans et al., 2001; Herwegh and Berger, 2004; Passchier,

35 2005; Karato, 2008; Herwegh et al., 2011; Hobbs et al., 2010). Microstructures of monomineralic aggregates are determined by the deformation behavior of the constituent mineral and by the physical conditions (e.g., temperature, stress, availability of fluids) existing during deformation. For example, Stipp et al. (2002) showed that the microstructures resulting from dynamic recrystallization of quartz can be linked to different recrystallization mechanisms active at increasing temperatures~~.~~ and strain rates. However, this type of interpretations is more complicated when dealing with polymineralic aggregates, where the ~~relative~~

40 ~~abundances~~modal amounts and specific deformation mechanisms of each mineral have an effect on the deformation behavior of the bulk ~~rock~~system (e.g., Handy, 1990; 1994; Olgaard, 1990; Stünitz and Fitz Gerald, 1993; Kruse and Stünitz, 1999; Tullis, 2002; Herwegh and Berger, 2004; Passchier, 2005; Herwegh et al., 2011; Wehrens et al., 2017). ~~As an example, it has been shown that the grain size of calcite in mylonitic carbonates is determined by the grain size and volume abundance of second phases, such as sheet silicates (Olgaard, 1990; Herwegh and Berger, 2004; Herwegh et al., 2011).~~ In this context, mass

45 transfer processes like dissolution–precipitation play a fundamental role in that they enable the redistribution of material within the deforming system (e.g., Paterson, 1995; Herwegh and Jenni, 2001; Konrad-Schmolke et al., 2018). ~~A circulating~~The essential requisite for dissolution–precipitation processes to occur is the presence of a fluid ~~may precipitate~~phase (e.g., Putnis, 2009; Putnis and Austrheim, 2010; Putnis and John, 2010). In the presence of a fluid, dissolved material ~~into~~may precipitate inside intragranular voids ~~of an initially monomineralic aggregate~~ during deformation. In this scenario, the process of

50 dissolution–precipitation in combination with the presence of a second phase keeps the grain sizes of the deforming aggregate small in a process called viscous granular flow (Olgaard, 1990; Fitz Gerald and Stünitz, 1993; Stünitz and Fitz Gerald, 1993; Paterson, 1995; Herwegh and Berger, 2004; Herwegh et al., 2011). Viscous granular flow ~~entails~~is a mechanism in which grains slide relative to one another: this process requires grain-size reduction, and plastic material transfer and/or dissolution–precipitation ~~that dissolves mineral asperities, thus facilitating~~processes (or solution transfer) at the scale of the deforming

55 polymineralic aggregate in order to facilitate grain boundary sliding ~~in polymineralic aggregates (e.g., Fitz Gerald and Stünitz, 1993; (~~Stünitz and Fitz Gerald, 1993; Paterson, 1995). Grain boundary sliding promotes the formation of creep cavities, hence allowing the nucleation of second-phase minerals (e.g., Herwegh and Jenni, 2001; Fusseis et al., 2009; Gilgannon et al., 2021). ~~Despite the important~~Fluids play a crucial role ~~of fluids involved~~ in deformation processes, ~~their direct characterization is rare (e.g., Marquer and Burkhard, 1992; Marquer and Peucat, 1994), and~~but it is often unclear whether the fluids are newly added

60 to the system during deformation (i.e., of external origin) or ~~if~~they are recycled (e.g., via dissolution of hydrous minerals).

Hence, the interplay of recycled and newly added fluids, mass-transfer processes and deformation mechanisms to produce complex microstructures remains to be fully appreciated.

In this contribution, via combined microstructural observations ~~and~~ geochemical data and Pb–Sr isotope geochemistry, we investigate the deformational processes affecting epidote ~~([~~i.e., $Ca_2Al_2(Al,Fe^{3+})Si_3O_{12}(OH)$~~) and quartz defining a microfold)]~~ in a ~~deformed~~folded epidote-quartz hydrothermal vein. ~~The data demonstrate that the present-day microstructure is the result of the interplay between dissolution–precipitation of epidote and dynamic recrystallization of quartz, both of which ensure grain size reduction in viscous granular flow.~~ deformed by shearing. The nature of the fluid ~~mediating dissolution–precipitation of epidote and the dynamic recrystallization of quartz~~assisting folding is investigated using Pb– and Sr isotope data. ~~Because epidote is a~~Epidote group minerals are widespread rock-forming, hydrothermal and alteration ~~mineral~~minerals in granitic rocks (e.g., Bird and Spieler, 2004; Enami et al., 2004; Franz and Liebscher, 2004; Grapes and Hoskin, 2004; Schmidt and Poli, 2004; Morad et al., 2010; Hentschel et al., ~~2020),~~2020), and they allegedly behave similarly during deformation. Therefore, the occurrence of epidote dissolution–precipitation and its control on the deformation mechanisms of other rock-forming minerals ~~(e.g., dislocation creep in quartz)~~ has important implications for the structural evolution of ~~the granitic continental crust~~granitoids, among other epidote-bearing rocks, during orogenic phases.

~~Figure 1: (a) Geological map of the Grimsel Pass area (modified from Wehrens et al., 2016). (b) Geographic location of the Grimsel Pass area (red star) in Switzerland (modified from map.geo.admin.ch).~~

Figure 1: (a) Geological map of the Grimsel Pass area (redrawn from Wehrens et al., 2016). (b) Geographic location of the Grimsel Pass area (red star) in Switzerland (modified from map.geo.admin.ch). The digital elevation model in panel a is from map.geo.admin.ch.

2 Geological Setting

The Grimsel Pass area (Fig. 1; central Swiss Alps, Switzerland) is in the southern part of the Aar Massif, one of the External Crystalline Massifs of the Alps (e.g., Schneeberger et al., 2019; Berger et al., 2017). The Aar Massif consists of a ~~polycyclic~~Paleozoic polymetamorphic basement and Permian intrusives, including the post-Variscan Central Aar Granite. This granitoid was emplaced 299 ± 2 Ma (Schaltegger & Corfu, 1992~~) and mainly records~~; Ruiz et al., 2022) and bears clear evidence for Alpine deformation (e.g., Choukroune and Gapais, 1983; Bambauer et al., 2009; and references therein). This Alpine deformation is expressed by a large number of ductile shear zones, and in the southern Aar Massif it can be subdivided
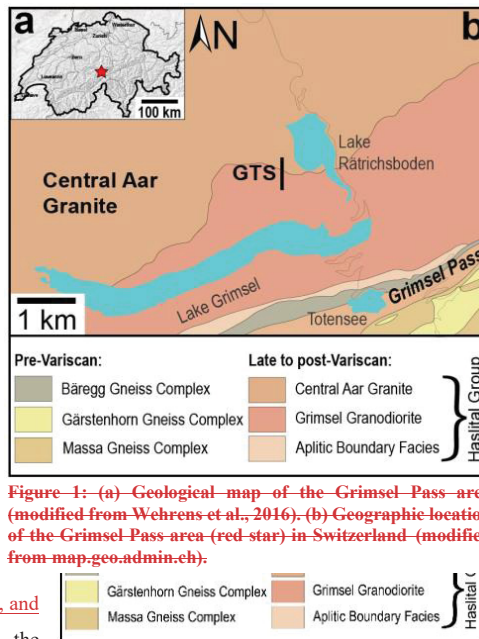
3

into two major phases: (1) a reverse faulting phase ~~(ca.~~with green biotite stable in the shear zones at < 400 °C (ca. 22–17 Ma; Challandes et al., 2008; Rolland et al., 2009; Wehrens et al.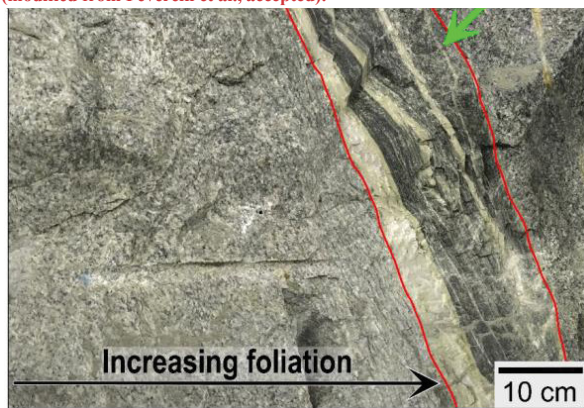, 2017) and (2) a strike-slip phase at lower temperatures with chlorite progressively replacing biotite in the shear zones (from ca. 14 Ma onwards; Rolland et al., 2009; Wehrens et al., 2017; Herwegh et al., 2020). ~~In the shear zones, green biotite is stable in the first phase at ≥ 400 °C, and it is progressively replaced by chlorite in the second one at lower temperatures (Rolland et al., 2009; Wehrens et al., 2017).~~ The Alpine metamorphic overprint reached greenschist facies conditions in the area, with maximum temperatures and pressures of 450 ± 30 °C and 6 ± 1 kbar, respectively (Challandes et al., 2008; Goncalves et al., 2012; Villa and Hanchar, 2013). Hydrothermal activity upon exhumation in Alpine times is recorded in the area primarily by the Grimsel Breccia Fault hydrothermal system (e.g., Hofmann et al., 2004; Belgrano et al., 2016; Diamond et al., 2018; Egli et al., 2018~~), and by Alpine~~). U–Pb geochronology of hydrothermal epidote in veins returned Miocene ages (19.2 ± 4.3 Ma and 16.9 ± 3.7 Ma; Peverelli et al., 2021) related to fluid circulation occurring during the Alpine orogenic phases, already described also on the basis of cleft mineralization (e.g., Mullis et al., 1994; Janots et al., 2012; Berger et al., 2013; 2022; Rossi and Rolland, 2014; Bergemann et al., 2017; Ricchi et al., 2019). ~~U–Pb geochronology of hydrothermal~~In addition, Permian ages (279 ± 29 Ma, 291 ± 50 Ma and 275 ± 18 Ma) returned by other epidote ~~in~~ veins ~~returned Miocene and Permian ages (~~revealed pre-orogenic fluid circulation in the Grimsel Pass area (Peverelli et al., ~~2021; accepted~~2022).

4
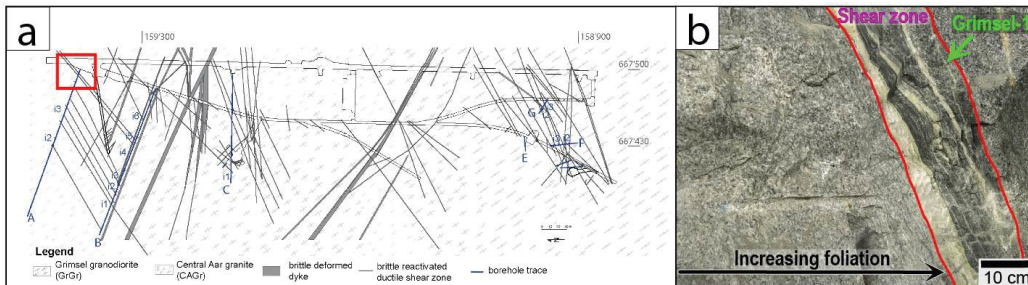
Figure 2: (a) Geological map of the Grimsel Test Site (GTS) of Nagra with the location of (b) shown in the red rectangle (redrawn from Schneeberger et al., 2019). (b) Field photograph of the location of the studied epidote-quartz vein (Grimsel-1) and the Alpine shear zone with which it is associated; both are in the Central Aar Granite, which shows increasing foliation towards the shear zone (modified from Peverelli et al., 2022).

3 Field relations and sample description

The investigated sample is called Grimsel-1 and it is an epidote-quartz (±biotite) vein that was collected in the Grimsel Pass area inside Nagra'sthe Grimsel Test Site (GTS; Figs. 1 2a), which is anthe underground rock laboratory in the Grimsel Pass area of Nagra (Figs. 1 and 2a). The GTS is a ca. 500 m long tunnel designed to study rock properties and fluid circulation in the area (see Schneeberger et al., 2019). In the GTS, the characteristicanastomosing pattern of shear zones (e.g., GoncalvesWehrens et al., 20122017) is well exposed on the tunnel walls. The studied epidote vein runs oblique with respect to is associated to a WSW–ENE-striking and a steeply NNW-dipping shear zone of Alpine age hosted by the Central Aar Granite (Fig. 2b). The shear zone is ca. 10 cm wide, whereas the epidote vein (Grimsel-1 in Fig. 2b) reaches up to a couple of centimeters in width. Three other epidote veins are associated with this shear zone (Fig. A1; not visible in Fig. 2b): (1) sample P2 is a weakly deformed epidote-quartz vein and ca. 50 cm in a slightly deformed portion oflength on the host; (2) sample P3 consists of a number of sheared epidote-quartz veins in a mylonitic portion; and (3) sample Gr0-c is a highly sheared epidote-quartz vein which subdivides the host rock into a mylonitic side and a slightly deformed one. Epidote in veins P2-3 returned Permian U-Pb ages (Peverelli et al., accepted). tunnel wall.

125

5

The ~~host~~ Central Aar Granite is the vein host and it displays a gradation from slightly to highly deformed: this is expressed by ~~an~~ increasingly intense foliation and ~~by a~~ decreasing grain size moving towards the shear zone (Fig. 2b). In thin section (Fig. 3), the host rock mostly preserves its magmatic texture and it is made of ca. 55 vol. % of altered feldspar and 35 vol. % quartz. Feldspar grains are sometimes fractured~~, and quartz is mostly dynamically recrystallized by subgrain rotation recrystallization (SGR).~~. Relict plagioclase and K-feldspar grains can be recognized by the different type and extent of alteration. Plagioclase (ca. 20 vol. %) is highly altered into epidote and white mica, to a larger extent in the cores than in the rims of the grains. Exsolution lamellae are preserved in K-feldspar grains (ca. 35 vol. %), which are moderately altered into sericite. Green biotite, epidote and minor chlorite define a weak foliation and make up ca. 10 vol. %, with a few accessory titanite grains completing the host rock's mineral assemblage. ~~The sharp boundary between host and vein is marked by a change in modal abundances.~~A detailed description of the host rock is outside the scope of this contribution and it is presented in Schneeberger et al. (2009).

The sharp boundary between host and vein is marked by a change in modal abundances in epidote and quartz. The object of the present investigation is Grimsel-1 epidote-quartz vein (Fig. ~~3).~~3; already used in Peverelli et al., 2021; 2022). This vein is subdivided into three layers: (1) layer with coarse-grained epidote~~,~~ (Fig. 4d), quartz and minor green biotite, (2) heavily deformed and
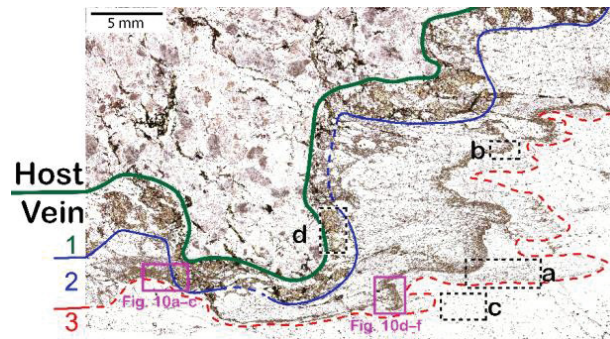

Figure 3: Transmitted-light microscope scan of the studied epidote-quartz (±biotite) vein and the host Central Aar Granite. The numbers 1–3 refer to the vein layers described in Sect. 3. Dashed rectangles a–d indicate the locations of the microstructural domains shown in Fig. 4a–d. The pink rectangles indicates the location of Fig. 10a–c (rotated by 90° clockwise) and Fig. 10d–f (rotated by 180°). Plane-polarized light.
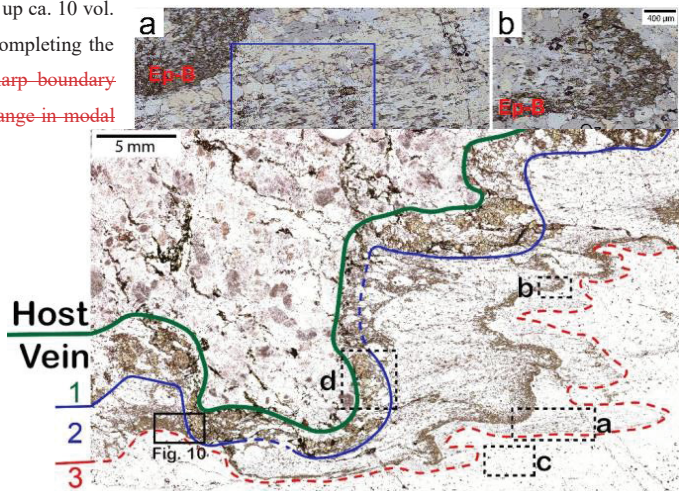

~~**Figure 3: Transmitted-light microscope scan of the studied epidote-quartz (±biotite) vein and the host Central Aar Granite. The numbers 1–3 refer to the vein layers described in Sect. 5.1. Dashed rectangles A–D indicate the locations of the microstructural domains shown in Fig. 4a–d. The black rectangle indicates the location of Fig. 10 (rotated by 90° clockwise). Plane-polarized light.**~~

finer-grained epidote-quartz layer, (Fig. 4a–b), and (3) nearly pure quartz layer. (Fig. 4c). Grain sizes, and mineral proportions and dominant deformation mechanisms in in each layer are given in Table 1. Layer 1 is the least Layers 2–3 are strongly deformed one, whilst deformation is most intense in layers 2–3, where a fold is defined and folded, as indicated by the spatial distribution of epidote and quartz (Fig Figs. 3). The reasons why layer 1 and 4b). Layer 1, on the other hand, is less deformed than layers 2–affected by this folding process (Figs. 3 may be linked to the closer proximity of layer 1 to the host rock, to a role of mechanically strong epidote clusters forming a load-bearing network, or to a combination of both (Handy, 1990; 1994; Masuda, 1990; 1995; Tullis, 2002; Passchier, 2005 and 4d). The modal abundance of green biotite varies greatly among the three layers, with a sharp decrease from layer 1 to layer 2, and layer 3 being devoid of biotite (Table 1). The transition from layer 2 to layer 3 is marked by a change in the epidote/quartz ratio. This is up to ca. 40/60 in layer 2, whereas layer 3 is characterized by the near absence of epidote. Peverelli et al. (2021; see their Fig. 6b) performed U–Pb dating by LA-ICP-MS of epidote grains in layer 1, obtaining a Tera–Wasserburg age of 19.2 ± 4.3 Ma. The Tera–Wasserburg regression revealed a single epidote generation at the current analytical precision (i.e., MSWD of 0.79), and the age is interpreted as the timing of epidote crystallization upon vein opening (Peverelli et al., 2021). The focus of this manuscript are the deformation mechanisms in layers 2–3.

Table 1: Main characteristics of the vein layers. Ep = epidote; SGR = subgrain rotation recrystallization; Qz = quartz; vol. = volume.

Layer	Minerals other than Ep + Qz	Ep [vol. %]	Ep grain size	Qz deformation	Qz grain size	Qz relicts
1	Green biotite (ca. 5 vol. %)	ca. 70	0.025–1.6 mm	Dislocation glide + SGR	80–400 µm	0.6–1.2 mm
2	Green biotite (ca. 1 vol. %)	ca. 5–40	5–90 µm	SGR + dislocation glide	20–170 µm	1.4–2.5 mm
3	-	< 1	5–200 µm	SGR + dislocation glide	30–400 µm	0.6–2 cm

4 Methods

Analyses were performed at the Institute of Geological Sciences of University of Bern (Switzerland) unless specified otherwise.). The petrographic characterization of the studied sample was done in a ca. 60 µm thick section on a Zeiss Axioplan petrographic microscope. For backscattered electron (BSE), forescattered electron (FSE) and cathodoluminescence (CL) images, and for electron backscatter diffraction (EBSD), a Zeiss EVO50 scanning electron microscope (SEM) was used with a beam current of ca. 1 nA and accelerating voltage of 20 kV.

Deleted Cells

4.1 Grain-size analysis

190 Microstructural analysis was performed combining transmission light and scanning electron microscopy to determine average grain sizes of epidote and quartz, as well as their volume fractions in selected microstructural domains. Grain size analysis was carried out in ImageJ (IJ 1.46r; Ferreira and Rasband, 2012) using sketches of the microstructures drawn on transmitted light, BSE and FSE images. In domains where the microstructure is not suitable for an automated grain size analysis by ImageJ (Figs. ~~4b and 7c), epidote and quartz grain sizes were directly measured on a transmitted light microscope.~~4b, 6 and 7c),

195 epidote and quartz areas were directly measured on a transmitted light microscope, approximated as ellipses. Epidote grains that are isolated among quartz grains are defined by the presence of epidote–quartz boundaries. Grain boundaries among or between epidote grains are defined as any irregular discontinuity between grains that is confirmed by different extinction angles at the optic microscope (i.e., misorientations of $\geq 2.5°$) QD tz grains are identified by the presence of visible grain boundaries in BSE images, and confirmed by observations of differences in extinction angles at the optic microscope. The

200 equivalent diameter of each grain (D) is calculated from the grain areas (A) as $D = 2 \times \sqrt{A/\pi}$.

4.2 Chemical maps

X-ray compositional maps in wave-length dispersive mode of Si, Fe, Al, Ca, Mn and Sr were obtained by electron probe micro-analyzer (EPMA) on a JEOL-8200 microprobe. Accelerating voltage was 15 keV, specimen current 100 nA, the step size 4 µm, and dwell time was 190 ~~msec.~~ms (map of layers 1–3; Fig. 10a–c) and 180 ms (map of layer 2; Fig. 10d–f). For calibration

205 of the X-ray maps, spot analyses were acquired with a specimen current of 10 nA, and calibrated using the following standards: wollastonite (SiO_2), olivine (MgO), anorthite (CaO, Al_2O_3), magnetite (FeO), pyrolusite (MnO), tugtupite (Cl), rutile (TiO_2), and celestite (SrO). The processing of the X-ray compositional maps, including map calibration, was done by using XMapTools (Lanari et al., 2014; 2019). Minerals were identified based on the concentrations of specific elements (i.e~~.,~~. Ca, Fe and Al for epidote; Si for quartz; K for micas) and classified. Maps of the structural formula of epidote were calculated on

210 12.5 oxygen basis.

4.3 Trace elements

For trace element measurements, a RESOlutionSE 193 nm excimer laser system (Applied Spectra, USA) equipped with an S-155 large-volume constant-geometry chamber (Laurin Technic, Australia) coupled with an Agilent 7900 ICP-QMS was employed. During ablation, a He atmosphere was used, and Ar was admixed to the carrier gas before reaching the plasma of

215 the ICP-MS. NIST SRM612 was used for optimization of the analytical conditions, ensuring that the ThO production rate was < 0.2 % and the Th/U sensitivity ratio > 97 %. On-sample fluence was 5 J cm^{-2} and repetition rate 5 Hz. The size of the analysis spots ranged between 20–30 µm, and BSE images were used to plan the analyses to avoid locating any spots across zones with heterogeneous composition (e.g., chemical zoning) or on inclusions. External standardization was done with USGS GSD-1G standard, and the SRM612 standard was measured as an unknown for quality control in absence of a well characterized epidote

8

Number: 1   Author: a Subject: Sticky Note   Date: 23/09/2022 17:02:17
Normally in literature grain boundaries are interpreted for misorientation > 10°.
Please, clarify what degree of misorientation you used to define grain boundaries and why.
If you adopt 10°, does it affect your data? If so, please update them.

220 standard. Bracketing standardization enabled a true-time linear drift correction. Data reduction was carried out with the software SILLS (Guillong et al., 2008), using the sum of total oxides minus H_2O (98.3 % for epidote and 100 % for SRM612) as internal standard (see Halter et al., 2002). The formulation of Pettke et al. (2012) was employed to calculate limits of detection for each element in every analysis.

4.4 U–Pb isotope data

225 Measurements of $^{238}U/^{206}Pb$, $^{207}Pb/^{206}Pb$ and(as well as) $^{87}Sr/^{86}Sr$; Sect. 4.5) were made in epidote micro-separates following the procedure for sample digestion in acids and for column chemistry detailed by Peverelli et al. (2021; modified from Nägler and Kamber, 1996). Two epidote micro-separates – each mixing Epidote-A and Epidote-B (see Sect. 5.1) in unknown and different proportions – were prepared (Ep_A+B_1 and Ep_A+B_2). After hand-picking, the material was finely ground and washed with MilliQ^{TM} water. Two aliquots of each (Ep_A+B_1a and Ep_A+B_1b, and Ep_A+B_2a and Ep_A+B_2b) were

230 weighed in as replicates for each micro-separate ensuring ca. 300 ng of Pb in each aliquot. During column chemistry with a Sr-spec^{TM} resin (Horwitz et al., 1992), the Sr and Pb fractions were collected in sequence (Haeusler et al., 2016). One large Epidote-A grain was also handpicked and ground, and an amount of the powder corresponding to 250 ng of Sr was digested in acids before the extraction of the Sr fraction by column chemistry. The Pb fraction of this Epidote-A grain was not collected since Pb isotopic data are available from in-situ U–Pb isotope measurements by LA-ICP-MS (Peverelli et al., 2021). Procedural

235 blank samples were used to assess contamination during work in the laboratories. ~~Measurements of ^{238}U and ^{206}Pb concentrations for calculation of $^{238}U/^{206}Pb$ ratios were run at the Department of Geography of University of Bern on a 7700x Agilent quadrupole ICP-MS. For these analyses, two aliquots of each digested epidote microseparate were separated and diluted to different volumes. Three aliquots were separated from the digested AGV-2 standard and diluted in 0.05, 0.25 and 0.7 ml HNO$_3$. The intensities in counts per second (cps) of ^{238}U and ^{206}Pb measured in the three aliquots of the AGV-2 standard~~

240 ~~were plotted against the real concentrations of these isotopes in ppb calculated for each aliquot using the reference data of Weis et al. (2006). The calibration curves thus obtained were used to calculate the real concentrations of ^{238}U and ^{206}Pb in the digested epidote material. The calculation of 2 standard errors (2 S.E.) on $^{238}U/^{206}Pb$ ratios – which are not returned automatically by the measurement software – is detailed in Peverelli et al. (2021).~~ PbLead isotope ratios were measured on a Thermo Fisher Neptune Plus MC-ICP-MS in desolvated plasma mode equipped with a CETAC Aridus 2 desolvating system.

245 Instrumental mass fractionation was corrected within-run by means of a Tl spike. External reproducibility of the measurements was quantified by measuring the NIST ~~NBS 981~~NBS981 standard. The measured Pb isotope ratios were identical to those obtained by Rehkämper and Mezger (2000; their Table 4).

9

4.5 Strontium isotope data

Strontium isotope ratios were measured on a ThermoFisher Triton^{TM} thermal ionization mass spectrometer (TIMS) after loading 250 ng Sr diluted in 6.4 M HCl on Re filaments using 1.5 µl Ta-oxide activator. The ~~SRM 987~~SRM987 standard (200 ppm; Weis et al., 2006) was measured for quality control. The detected masses were 84, 85, 86 (center cup), 87 and 88. The interference of ^{87}Rb and within-run mass fractionation were corrected for by using the IUPAC ^{87}Rb/^{85}Rb and ^{88}Sr/^{86}Sr values of, respectively, 0.385617 and 8.735209. The ~~SRM 987~~SRM987 standard returned a weighted average ^{87}Sr/^{86}Sr ratio of 0.710279 ± 0.000020 (2 standard deviation, ~~S.D.;~~SD; number of replicates, n = 12), which is higher than the reference preferred value of 0.710248 (see Weis et al., 2006). Standards AGV-2 (n = 1) and GSP-2 (n = 2) of USGS were measured as unknowns for quality control and the returned, respectively, ^{87}Sr/^{86}Sr ratios of 0.704041 ± 0.000018 (2 standard error, 2 ~~S.E.),~~ ~~and 0.765396 ± 0.000010~~SE) and 0.765202 ± 0.000008. These

Figure 4: ~~Transmitted-light scans of the microstructural domains described in Sect. 5.1. Microstructures (a–c) are used for microstructural analysis (Fig. 7; Sect. 5.1.2). The blue rectangle in (a) indicates the location of the cathodoluminescence image of Fig. 11. Bt = biotite; Ep = epidote; Fsp = feldspar; Qz = quartz. Plane-polarized light.~~

Figure 5: Details of epidote in layer 1. (a–b) Transmitted light microphotographs of epidote, dynamically recrystallized quartz and quartz; plane-polarized (a) and cross-polarized (b) light. (c) One isolated epidote grain surrounded by epidote clasts (red arrow). (d) Backscattered electron image of one epidote grain showing lobate grain boundaries and microporosity given by fluid inclusions (FIs). Bt = biotite; Ep = epidote; Qtz = quartz. Anomalous birefringence in panels a and c is due to the thickness of the thin section (ca. 60 µm).

values are also higher than the reference preferred values of 0.703981 ± 0.00009 (2 ~~S.D.)~~SD) and 0.765144 ± 0.000075 (2 ~~S.D.)~~SD) for AGV-2 and GSP-2, respectively (see Weis et al., 2006). A correction based on the reference materials returning higher ^{87}Sr/^{86}Sr values than their reference values would produce the same shift in all measured ^{87}Sr/^{86}Sr ratios. Hence, we did not correct our data because only the variability among the samples is relevant in this study, while the interpretation of the absolute Sr isotope ratios is beyond the scope of this work. Rubidium concentrations were not measured, as a correction for ^{87}Rb-derived ^{87}Sr is not necessary in epidote. This is a valid approach because the incompatibility of Rb in the epidote crystal structure results in negligible Rb concentrations (see Frei et al., 2004; Feineman et al., 2007).
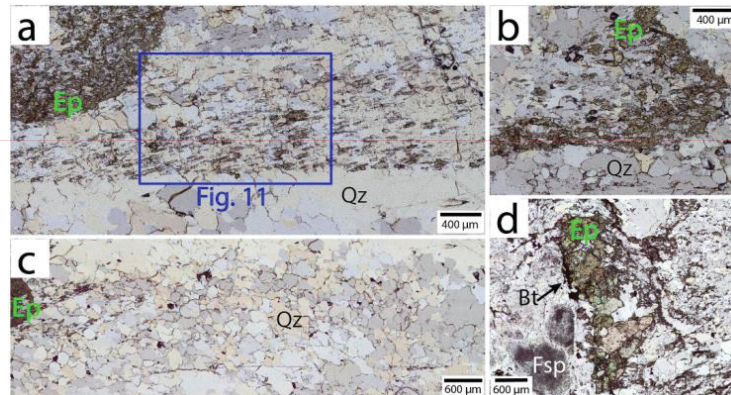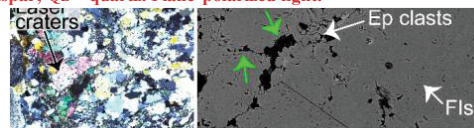
Number: 1   Author: a Subject: Sticky Note   Date: 23/09/2022 17:01:11
Maybe better:
Suggested by the presence of fluid inclusions?
FI are barely visible. If this is important, please improve

5 Results

5.1 Microstructural analysis

The different characteristics of epidote and its microstructures in layers 1–3 (Figs. 3–4) allow the distinction of epidote into Epidote-A and Epidote-B as illustrated below. ~~All~~The microstructural ~~domains indicate that vein opening with crystallization~~characteristics of epidote~~, quartz~~ – described below – suggest different formation mechanisms between epidote
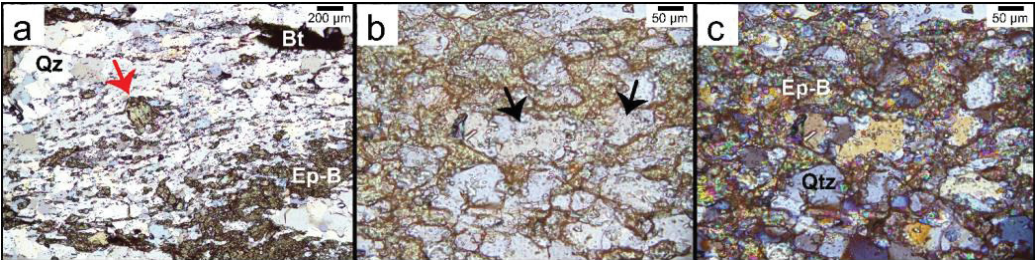

Figure 6: Transmitted light microphotographs of layer 2. (a) Detail of the epidote microfold, with oval epidote grains hosted by dynamically recrystallized quartz and their long axes oriented consistently with the microfold axial planes; red arrow: euhedral epidote grain. Overlapped imaged in plane-polarized and cross-polarized light. (b–c) Details of quartz enclosures among epidote grains in plane-polarized (b) and cross-polarized (c) light; the black arrows point at epidote and fluid inclusions in quartz. Bt = biotite; Ep = epidote; Qtz = quartz.

in layer 1 and ~~minor biotite was followed by vein deformation~~in layers 2–3.

5.1.1 Layer 1: veining and Epidote-A

~~This epidote layer~~Layer 1 is characterized by coarse (ca. 0.2–1.6 mm) epidote grains associated with smaller angular ones (ca. 20–200 μm). The coarser epidote grains (Figs. 4d and ~~5~~5a–b) form clusters with random shape orientations or are found as isolated crystals. Larger epidote grains are often surrounded by the smaller angular epidote grains (Fig. ~~5~~5c; red arrow) as a result of brittle grain-size reduction upon deformation with brittle deformation behavior of epidote. Epidote is euhedral to anhedral~~,~~. Anhedral/subhedral epidote has lobate grain boundaries (Fig. 5d), and smaller epidote crystals are found in the gaps among the larger ones as well ~~(see Fig. 2b of Peverelli et al., 2021). Large~~("Ep clasts" in Fig. 5d). Quartz is mostly dynamically
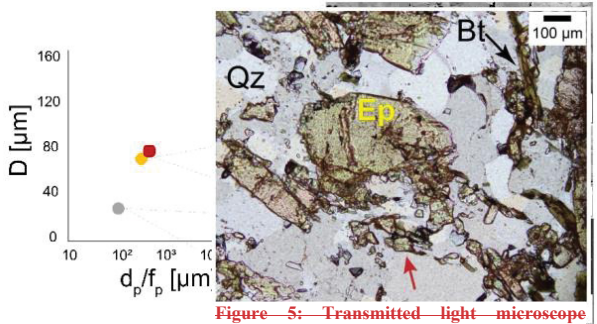

Figure 5: Transmitted light microscope photograph of one Epidote-A grain in layer 1 surrounded by small angular grains (red arrow). Bt = biotite; Ep = epidote; Qz = quartz. Plane-polarized light.

Figure 7: Correlation between ... (ratio between ... as the second ... detrital microstructures in the ... BSE image contour epidote grains. Ep = epidote; Qz = quartz. Panels a, b and c correspond, respectively, to panels b, a and c of Fig. 4.

11

Number: 1   Author: a Subject: Sticky Note   Date: 23/09/2022 17:04:47
Please, state here what this "second phase is".

recrystallized, although some large quartz relics are present displaying undulose extinction. ~~More commonly, quartz is dynamically recrystallized, forming core-mantle structures with subgrain rotation around quartz relics.~~ (Fig. 5a–b). Hereafter, we refer to epidote in layer 1 as Epidote-A.

5.1.2 Layers 2–3: microfold and Epidote-B

In layers 2–3, the spatial distribution and the variable modal abundance of epidote define a fold (Figs. 3, 4b, 6 and A1). Smaller epidote grains with a shape-preferred orientation and quartz define axial planes ~~and limbs~~ (rectangle a in Fig. 3; Figs. 4a and 6). Epidote grain boundaries are mostly curved and irregular, but a few subhedral or euhedral epidote grains are also observed (Fig. ~~6~~6a, red arrow). Epidote grains vary between 5–90
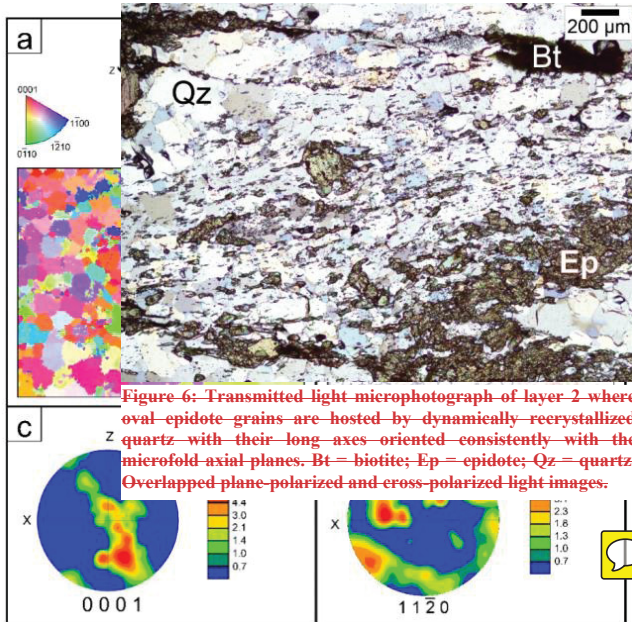

Figure 6: Transmitted light microphotograph of layer 2 where oval epidote grains are hosted by dynamically recrystallized quartz with their long axes oriented consistently with the microfold axial planes. Bt = biotite; Ep = epidote; Qz = quartz. Overlapped plane-polarized and cross-polarized light images.
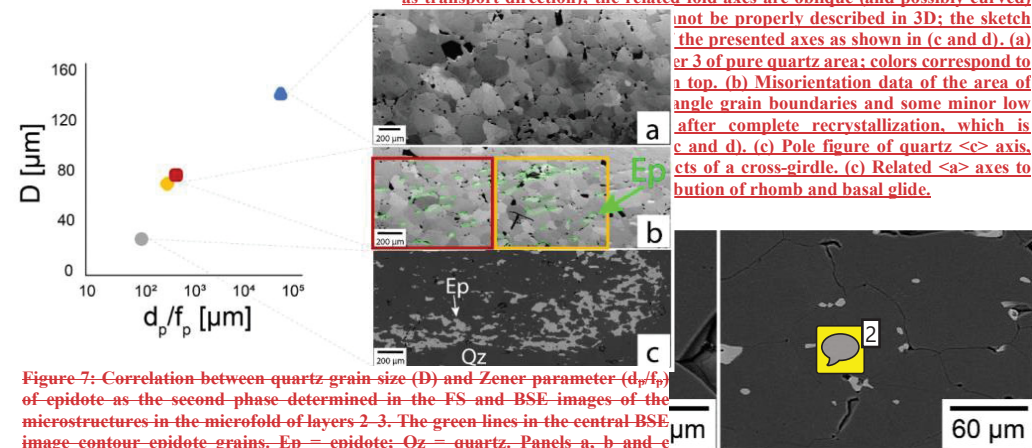
Figure 8: Crystallographic data of quartz in layer 3. (a, top part) The transpressional deformation produces shearing with some lineation (interpreted as transport direction); the related fold axes are oblique (and possibly curved) [...] not be properly described in 3D; the sketch [...] the presented axes as shown in (c and d). (a) [...] r 3 of pure quartz area; colors correspond to [...] top. (b) Misorientation data of the area of [...] angle grain boundaries and some minor low [...] after complete recrystallization, which is [...] c and d). (c) Pole figure of quartz <c> axis, [...] cts of a cross-girdle. (c) Related <a> axes to [...] bution of rhomb and basal glide.

Figure 7: Correlation between quartz grain size (D) and Zener parameter (d_p/f_p) of epidote as the second phase determined in the FS and BSE images of the microstructures in the microfold of layers 2–3. The green lines in the central BSE image contour epidote grains. Ep = epidote; Qz = quartz. Panels a, b and c correspond, respectively, to panels b, a and c of Fig. 4.

[...] ages showing epidote (Ep) grains along quartz (Qz) grain boundaries and at triple junctions among quartz grains.

12

Number: 1   Author: a Subject: Sticky Note   Date: 23/09/2022 16:46:50
What is the number of analysed grains?

Number: 2   Author: a Subject: Sticky Note   Date: 23/09/2022 17:06:09
In this image it seems that not all Ep grains are located at grain boundaries, some of those seem to be inside quartz grains.

320 µm in size, ~~and the~~hampering U–Pb dating of epidote in layers 2–3. The modal abundance of epidote varies between ca. 5 to
ca. 40 vol. % within the layer (Table 1), defining a quartz-supported microstructure. Where epidote is most abundant, quartz
~~and~~is confined as anhedral enclosures among epidote ~~define a "sponge-like" microstructure~~grains (Figs. 4b and ~~6~~6b–c). Small
(ca. 1–20 µm in size) oval epidote grains and fluid inclusions are observed within quartz grains (~~Figs. 4a and 6~~Fig. 6b–c). The
size of dynamically recrystallized quartz grains correlates with grain size and abundance of epidote (Fig. ~~7; Zener relation;~~
325 ~~Herwegh et al., 2010). Dynamic recrystallization of quartz by subgrain rotation prevails creating a crystallographic preferred~~
~~orientation (Fig. 8), and quartz relicts with undulose extinction are minor (Fig. 4a–c). However, a ca. 2 cm long relict quartz~~
~~grain, whose orientation acquired during crystallization may have favored dislocation glide, marks the transition from layer 2~~
~~to layer 3 (Fig. A1, black arrow).~~7). Such a relation, referred to as "Zener relation", shows interplay of grain sizes and related
energies/deformation mechanisms occurring in epidote and quartz simultaneously (see Herwegh et al., 2011; and references
330 therein). Dynamic recrystallization of quartz occurs by subgrain rotation (Figs. 4a–c and 7; compare with Stipp et al., 2002),
leading to a crystallographic preferred orientation (CPO; Fig. 8a). The investigated layers show almost complete
recrystallization, as indicated by the predominance of high boundary misorientations among quartz grains (Fig. 8b). The CPO
shows a weak <c> axis single girdle with related <a> axis distribution, but also relicts of a cross-girdle can be inferred (Fig.
8c–d). These CPOs are interpreted as basal and rhomb slip systems as seen in Schmid and Casey (1986; and references therein)
335 and Law (2014; and references therein). As discussed by Schmid and Casey (1986), the change from cross girdle <c> axis
distribution towards a single-girdle is related to the symmetry of deformation. Therefore, the <c> axes developed during pure
and simple shear deformation, which is already documented in the macrostructure (shearing and folding). A few quartz relicts
are recognized thanks to their undulose extinction (black arrows in Figs. 4a, 4c and Fig. A1). Where minor epidote is present,
anhedral epidote grains of few to ca. 10 µm in size are mostly interstitial and found at triple junctions among quartz subgrains
340 (Fig. 9). We refer to subhedral to anhedral epidote grains ~~defining the microfold in layers 2–3 as Epidote-B. While U–Pb ages~~
~~by LA-ICP-MS of Epidote-A (Sect. 3) are available, no U–Pb dating is possible in Epidote-B because the small grain size of~~
~~epidote entails contamination from epidote-epidote or epidote-quartz grain boundaries upon measurements~~in the microfold in
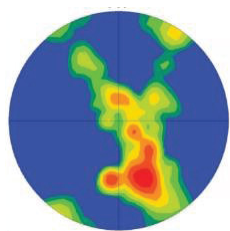layers 2–3 as Epidote-B.

5.2 Major and minor elements

The compositional ~~map~~maps in Fig. 10 (~~location~~locations shown in Fig. 3) ~~covers~~include layers 1–3, as marked in the figure. The compositions of FeO and Mn range between ca. 12.5–14 wt. % and ca. 2500–5000 µg g^{-1}, respectively, across all analyzed epidote grains. Larger Epidote-A grains in layer 1 are zoned, with FeO and Mn concentrations increasing from core to rim. Epidote in layers 2–3, on the other end, is characterized by uniform concentrations of FeO and Mn. It should be noted that, because the step size of the compositional maps is 4 µm, the chemical variability of epidote in layers 2–3 is better assessed among different grains across the overall microstructure rather than within each crystal (i.e., the majority of grains do not contain enough 4×4 µm pixels).
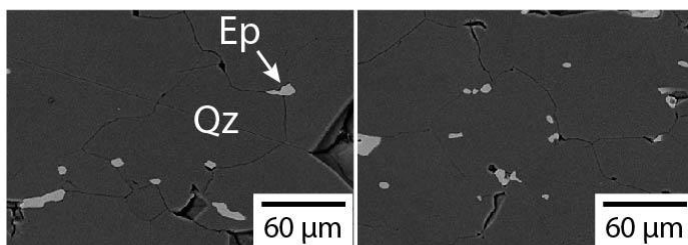

Figure 10: (a–c) Compositi~~indicate spots for U–Pb~~ Compositional maps of lay~~o~~ by the red curves.

5.2 Trace elements

The minimum spot size used for measurements by LA-ICP-MS is 20 µm, which is ca. four times larger than the smallest epidote grains. Therefore, chemical variability is assessed throughout each microstructural layer by relying on measurements in large-enough epidote grains to avoid contamination from grain boundaries. Epidote-A is also addressed here with no specific reference to intra-grain zoning but only across the overall Epidote-A microstructure (i.e., layer 1). Data of Epidote-B are collected in anhedral epidote grains in layer 2. The different extents of chemical variability between Epidote-A and Epidote-B noted in the compositional maps (Fig. 10) is reflected by trace element data (Fig.11; Table 2).

The concentrations of Sr and Pb in Epidote-B overlap with the trend defined by the same elements measured in Epidote-A, but they cover a more limited range of values (Fig. 11a). The CI chondrite-normalized rare earth elements (REE) patterns (Fig. 11b) of Epidote-A and Epidote-B have similar trends, characterized by positive slopes (La_N/Yb_N of 0.1–0.4 in Epidote-A and 0.03–0.5 in Epidote-B) and variably positive Eu anomalies (1.5–2.4 in Epidote-A and 1.2–2.3 in Epidote-B). The REE trends of Epidote-B fall within the range of Epidote-A and confirm the lesser extent of chemical variability of Epidote-B relative to
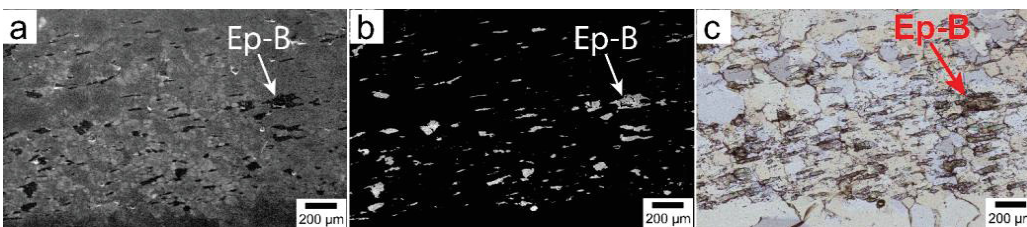
Figure 12: Cathodoluminescence (CL; a) and backscattered electron images (b) of the microstructural domain in the transmitted light microphotograph of panel c. The only minerals in the images are epidote (Ep) and quartz (unlabeled grains). The different CL contrasts in quartz (a) are due to variable trace element contents. The anomalous birefringence in panel c is due to the thickness of the thin section (ca. 60 µm).

Epidote-A. Selected elements, plotted as values normalized to the concentrations in the vein's host Central Aar Granite in Fig.

15

380 11c, reinforce chemical affinity between Epidote-A and Epidote-B, as well as the lesser chemical variability of the latter relative to the former. Cathodoluminescence images of the recrystallized quartz grains (Fig. 12) qualitatively indicate trace element variability also in quartz grains (see Ramseyer et al., 1988; Götze et al., 2001; Nègre et al., 2022).
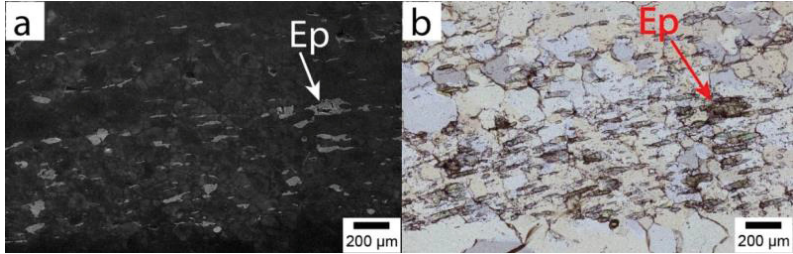

Figure 12: Overlapped cathodoluminescence CL) and backscattered electron images. The only minerals in the image are epidote (Ep) and quartz (unlabeled grains). The different CL contrasts in quartz are due to variable trace element contents.

Table 2: Trace element composition of epidote in µg g⁻¹measured by LA-ICP-MS.

Spot	Ba	Sr	Pb	U	La	Ce	Pr	Nd	Sm	Eu	Gd	Tb	Dy	Y	Ho	Er	Tm	Yb	Lu	Zr	V
Epidote-A																					
1	0.99	1400	130	79	5.6	14	2.2	12	6.3	3.9	14	2.8	22	200	5.5	19	2.7	19	2.7	3.6	140
2	1.2	1990	130	130	7.7	18	2.7	15	8.5	5.6	18	3.6	27	230	6.4	22	3.1	21	3.4	5.1	140
3	22	3290	150	350	4.8	8.8	1.2	5.6	2.5	2.0	5.7	1.2	12	120	3.6	14	2.5	21	3.8	22	110
4	21	2500	170	270	0.99	1.9	0.24	1.1	0.66	1.1	2.8	0.86	9.8	110	3.1	14	2.7	23	4.4	24	110
5	1.9	970	97	60	5.2	9.3	1.1	5.0	1.8	1.3	2.9	0.62	5.1	32	1.0	3.5	0.53	3.7	0.57	4.2	160
6	23	2590	170	130	10	15	1.6	7.0	2.8	1.9	5.6	1.3	9.9	71	2.3	9.2	1.6	15	3.1	51	130
7	0.98	740	87	140	5.0	9.3	1.2	5.3	2.7	1.6	4.5	1.1	8.4	53	1.8	6.0	0.88	5.8	0.77	4.5	200
8	21	2870	170	240	12	17	1.8	8.3	4.6	3.7	11	2.5	19	130	4.4	17	2.8	25	4.4	17	150
9	9.7	2000	150	100	8.5	12	1.4	5.9	3.2	2.7	8.0	1.8	14	82	2.9	8.7	1.1	7.8	1.3	9.6	140
10	24	2890	170	220	9.7		1.1	4.6	2.0	2.2	5.9	1.4	12	90	2.9	11	2.1	18	3.2	31	140
11	0.92	1660	93	100	3.4	7.2	0.90	3.3	1.2	1.4	2.7	0.59	5.1	41	1.3	4.1	0.42	2.5	0.28	2.2	110
12	34	3750	190	140	5.3	8.5	1.0	4.6	1.9	2.3	4.2	1.0	8.8	67	2.2	6.7	0.80	4.8	0.64	25	120
13	0.59	770	78	160	1.6	3.0	0.39	1.6	1.0	1.5	3.2	1.0	9.1	65	2.2	7.9	0.97	5.9	0.72	3.2	180
14	27	2820	180	260	1.3	2.5	0.29	1.2	1.2	1.5	4.6	1.3	12	120	3.5	14	2.8	28	4.6	42	130
15	5.8	1530	93	54	0.62	0.97	0.12	0.62	0.45	0.94	1.4	0.40	4.1	42	1.2	4.7	0.77	6.2	1.0	5.0	140
16	17	2810	150	140	1.9	3.0	0.35	1.4	0.55	1.3	1.7	0.66	7.8	77	2.3	9.3	1.6	14	2.3	18	130
17	5.2	1310	93	120	3.5	6.3	0.78	3.7	1.3	1.4	2.0	0.57	4.9	47	1.3	6.1	0.88	7.1	0.93	5.2	120
18	3.8	2340	110	110	1.5	2.9	0.43	1.6	0.76	1.2	1.6	0.47	4.9	47	5.5	5.5	0.78	5.8	0.90	3.1	120
Epidote-B																					
1	2.1	1640	171	130	4.7	10	1.4	7.1	3.4	3.0	7.3	1.7	16	150	4.4	14	2.1	14	2.3	5.2	130
2	2.9	1860	150	140	3.7	8.1	1.1	5.7	3.1	3.1	7.6	2.1	17	170	4.6	16	2.4	19	3.0	5.9	140
3	6.6	1950	120	190	1.7	4.2	0.55	2.9	1.2	1.6	3.1	0.81	8.1	85	2.1	8.6	1.5	9.7	1.7	8.2	120
4	5.0	1720	140	190	3.3	7.6	1.1	5.2	2.4	2.0	4.8	1.1	10	110	3.1	11	1.8	13	2.1	7.0	120
5	4.2	1700	130	170	3.0	7.4	0.97	5.0	2.3	2.1	4.2	1.2	11	120	3.0	11	2.0	14	2.5	7.7	120
6	5.1	1930	120	160	1.9	4.4	0.60	2.9	1.4	1.5	3.3	0.80	7.4	85	2.3	8.8	1.3	10	1.6	7.2	130
7	3.7	1530	130	160	2.9	6.6	0.88	4.5	2.1	1.7	4.1	0.73	7.9	84	2.3	8.3	1.3	9.0	1.6	5.2	130
8	6.5	1960	140	190	3.3	7.6	0.99	4.5	2.3	1.9	3.9	0.99	9.1	100	2.6	10	1.5	13	2.1	9.3	130
9	5.3	1850	130	190	3.4	8.2	1.1	4.7	2.2	1.9	3.7	0.91	8.4	100	2.7	9.9	1.5	13	2.1	8.6	130
10	5.4	1800	130	190	2.3	5.2	0.71	3.5	1.7	1.7	3.6	0.85	8.5	90	2.4	10	1.7	12	2.2	8.1	130
11	5.5	1800	150	180	3.9	8.5	1.2	5.6	2.5	1.9	4.9	0.99	9.8	100	2.7	10	1.6	12	1.9	8.0	130
12	4.8	1710	151	230	9.4	20	2.6	12	5.3	3.5	9.6	2.3	19	160	4.8	16	2.4	16	2.6	7.6	130
Central Aar Granite (Schaltegger and Krähenbühl, 1990)																					
KAW 2219	430	75	24	8	26	61	-	-	5.1	0.51	-	2.4	-	56	-	-	-	8.6	12	192	18

The concentrations of Sr and Pb in Epidote-B overlap with the trend defined by the same elements measured in Epidote-A, but they cover a more limited range of values (Fig. 11a). The CI chondrite-normalized rare earth elements (REE) patterns (Fig.

~~11b) of Epidote-A and Epidote-B have similar trends, characterized by positive slopes (La_N/Yb_N of 0.1–0.4 in Epidote-A and 0.03–0.5 in Epidote-B) and variably positive Eu anomalies (1.5–2.4 in Epidote-A and 1.2–2.3 in Epidote-B). The REE trends of Epidote-B fall within the~~
~~range of Epidote-A and confirm the lesser extent of chemical variability of Epidote-B relative to Epidote-A. Selected elements are plotted as values normalized to the concentrations in the Central Aar Granite in Fig. 11d reinforce chemical affinity between Epidote-A and~~
~~Epidote-B, as well as the lesser chemical variability of the latter relative to the former. Cathodoluminescence images of the recrystallized quartz grains (Fig. 12) qualitatively indicate trace element variability also in quartz grains~~.
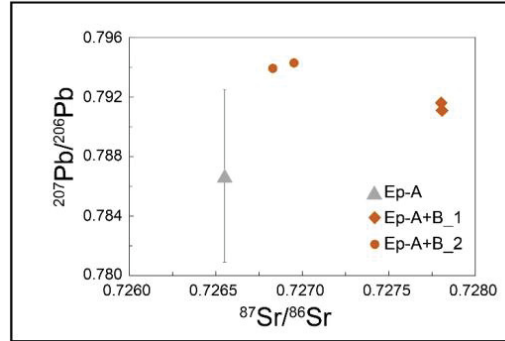

Figure 13: Total $^{207}Pb/^{206}Pb$ and initial $^{87}Sr/^{86}Sr$ data of Epidote-A and the epidote micro-separates; the $^{207}Pb/^{206}Pb$ ratio of Epidote-A is by LA-ICP-MS (analysis #10 of Peverelli et al., 2021); all other $^{207}Pb/^{206}Pb$ ratios are by solution ICP-MS; $^{87}Sr/^{86}Sr$ ratios are by TIMS; error bars are smaller than the symbols where not shown.

5.3 Isotope data

410 Strontium and Pb isotopic data (Table 2) of the epidote microseparates and those of the Epidote-A grain are plotted in Fig. 13. To compare the Pb and Sr isotopic composition of Epidote-A with those of the micro-separates mixing Epidote-A and Epidote-B, data obtained from three different techniques are combined in one $^{207}Pb/^{206}Pb$ versus $^{87}Sr/^{86}Sr$ plot. All $^{87}Sr/^{86}Sr$ ratios and the $^{207}Pb/^{206}Pb$ ratios of the micro-separates mixing Epidote-A and Epidote-B were measured by bulk techniques – namely TIMS and solution ICP-MS – which homogenize ca. 9×10^9 μm^3 of epidote material. Epidote-A $^{207}Pb/^{206}Pb$ ratios are taken

415 from LA-ICP-MS measurements by Peverelli et al. (2021), which include 23 in-situ analyses sampling ca. $20–24 \times 10^3$ m^3 each. The small volume of epidote material sampled in LA-ICP-MS analyses causes much larger variation among the single $^{207}Pb/^{206}Pb$ analyses. In order to plot one datum-point for each micro-separate aliquot against one representing the Epidote-A end-member, an average $^{207}Pb/^{206}Pb$ ratio has to be calculated from the LA-ICP-MS data-points. To obtain one datum-point for Epidote-A, thus, we use analysis #10 of Peverelli et al. (2021; see their Table 5) to represent the $^{207}Pb/^{206}Pb$ ratio of Epidote-

420 A in combination with the $^{87}Sr/^{86}Sr$ ratio measured by TIMS (Table 3). This is the datum-point closest to the average (0.786) and to the median (0.787) values of the $^{207}Pb/^{206}Pb$ ratios measured by LA-ICP-MS, hence the best representative value of $^{207}Pb/^{206}Pb$ in Epidote-A. It should be noted that there is a fundamental difference between the Pb and Sr isotope systems in

epidote: Sr isotopes reflect the Sr isotope composition of the fluid, given the negligible Rb contents of epidote. In contrast, the measured ^{207}Pb/^{206}Pb ratios contain both initial (i.e., inherited from the fluid during crystallization) and radiogenic (i.e., ingrown U-derived after crystallization) Pb. Therefore, Fig. 13 is a plot of total (initial + radiogenic) ^{207}Pb/^{206}Pb vs. initial ^{87}Sr/^{86}Sr ratios.
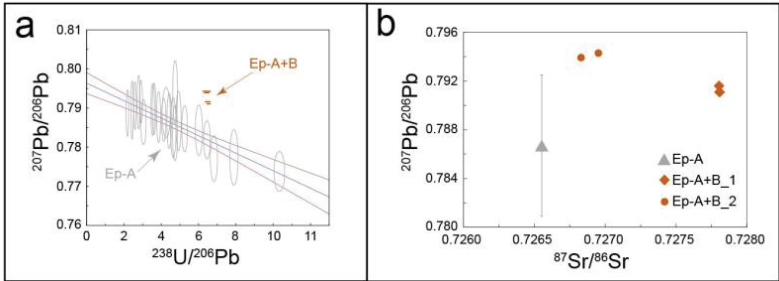

Figure 13: U–Pb and Sr isotope data. (a) Tera–Wasserburg diagram with the LA-ICP-MS data measured in Epidote-A (Ep-A) by Peverelli et al. (2021) and those measured in epidote microseparates (Ep-A+B) by solution ICP-MS; LA-ICP-MS error ellipses are 2σ. (b) Total ^{207}Pb/^{206}Pb and initial ^{87}Sr/^{86}Sr data of Epidote-A and the epidote microseparates; the ^{207}Pb/^{206}Pb ratio of Epidote-A is by LA-ICP-MS (data-point #10 of Peverelli et al., 2021); all other ^{207}Pb/^{206}Pb ratios are by solution ICP-MS; ^{87}Sr/^{86}Sr ratios are by TIMS; error bars are smaller than the symbols where not shown.

Table 3: U–Pb and Sr isotopic data by solution ICP-MS and TIMS. Uncertainties are 2 standard errors (2 S.E.).

	^{238}U/^{206}Pb	2 S.E.	^{207}Pb/^{206}Pb	2 S.E.	^{87}Sr/^{86}Sr	2 S.E.
Ep_A+B_1a	6.49	0.11	0.79159	0.00001	0.727803	0.000011
Ep_A+B_1b	6.54	0.07	0.79108	0.00001	0.727807	0.000007
Ep_A+B_2a	6.44	0.16	0.79428	0.00001	0.726952	0.000010
Ep_A+B_2b	6.44	0.10	0.79391	0.00001	0.726830	0.000015
Epidote-A	4.42[1]	0.09[1]	0.7867[1]	0.0058[1]	0.726552	0.000007

[1] Datum-point #10 of Peverelli et al. (2021) by LA-ICP-MS.

The total ^{238}U/^{206}Pb and ^{207}Pb/^{206}Pb ratios measured by solution ICP-MS in the epidote microseparates (Table 3) are plotted in a Tera–Wasserburg diagram (Fig. 13a) together with the LA-ICP-MS data measured in Epidote-A. The ^{238}U/^{206}Pb ratios of the dry aliquots of each microseparate are within uncertainty of each other, whereas their ^{207}Pb/^{206}Pb ratios are slightly different. This is attributed to geological heterogeneity between the single aliquots of each microseparate: perfect homogenization of the microseparates is not possible because total ^{207}Pb/^{206}Pb ratios include uranogenic lead in addition to initial Pb, and are therefore influenced by the variability in U concentrations. The solution ICP-MS data-points plot above the regression through the LA-

18

ICP-MS data in the diagram, and the isotopic ratios measured by the different techniques cannot be combined in one single regression.

445   Strontium (Table 3) and Pb isotopic data of the epidote microseparates and of pure epidote (Epidote-A) are plotted in Fig. 13b. To compare the Pb and Sr isotopic characteristics of Epidote-A with those of the microseparates, data obtained from the different techniques have to be combined in a $^{207}Pb/^{206}Pb$ versus $^{87}Sr/^{86}Sr$ plot. While Sr in epidote is entirely non-radiogenic, the $^{207}Pb/^{206}Pb$ ratios measured by solution ICP-MS contain both initial and radiogenic (i.e., U-derived) Pb. Therefore, to discuss Pb isotopic characteristics of Epidote-A (i.e., analyzed by LA-ICP-MS) against those of the epidote microseparates

450   mixing Epidote-A and Epidote-B (i.e., analyzed by solution ICP-MS), we cannot simply use the initial $^{207}Pb/^{206}Pb$ ratio obtained from a Tera-Wasserburg plot because this value excludes the ingrown radiogenic Pb component of Epidote-A. Therefore, in a $^{207}Pb/^{206}Pb$ versus $^{87}Sr/^{86}Sr$ plot (Fig. 13b), the total $^{207}Pb/^{206}Pb$ ratio of Epidote-A is represented by analysis #10 of Peverelli et al. (2021; see their Table 5). This is the datum-point closest to the average ($^{238}U/^{206}Pb = 4.62$ and $^{207}Pb/^{206}Pb = 0.786$) and to the median ($^{238}U/^{206}Pb = 4.35$ and $^{207}Pb/^{206}Pb = 0.787$) values of the U-Pb isotopic ratios measured in Epidote-

455   A by LA-ICP-MS.

6 Discussion of the formation mechanisms for the epidote-quartz microfold

6.1 Interplay of epidote dissolution–precipitation and quartz dynamic recrystallization

The formation of a hydrothermal vein entails the crystallization of a mineral assemblage from a mineralizing fluid that fills a fracture (Bons et al., 2012). Although the original morphology of the studied epidote-quartz vein is obliterated by deformation, the euhedral, often elongate, shapes of Epidote-A grains (Fig. 4d) suggest that the formation of Epidote-A in layer 1 is related to vein-filling mineralization, with crystallization occurring in equilibrium with a fluid. While the formation of Epidote-A is ascribed to veining, in the following we address the mechanisms affecting Epidote-B. as observed in less deformed epidote veins (e.g., Figs. 1a and 1c of Peverelli et al., 2021) and in other vein-filling minerals (e.g., Oliver and Bons, 2001; Bons et al., 2012; and references therein). The reasons why layer 1 is less deformed than layers 2–
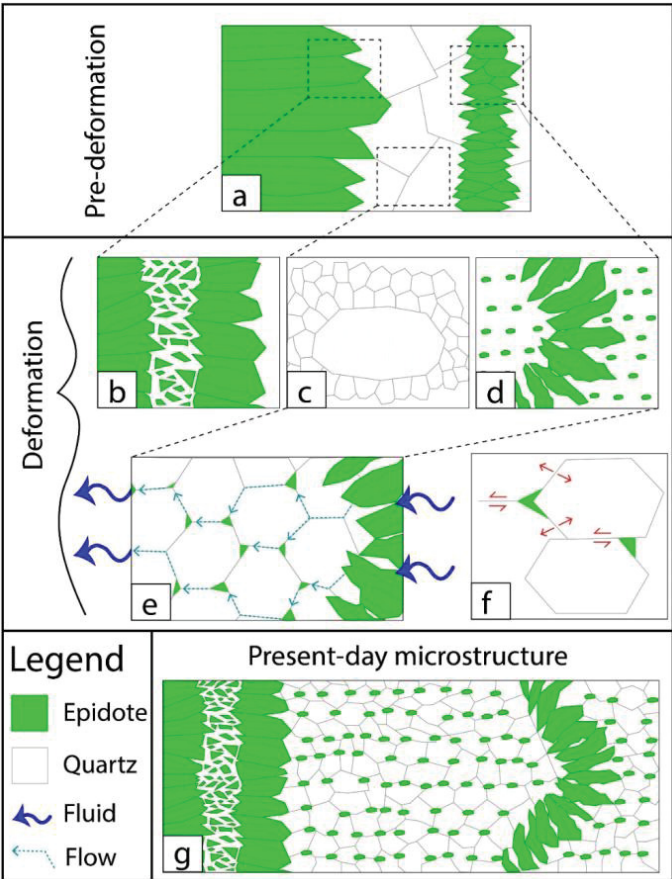

Figure 14: Sketch of the sequence of events affecting the studied epidote vein. (a) Original microstructure formed upon veining. (b) Detail of the fracturing occurring in Epidote-A in layer 1. (c) Dynamic recrystallization of quartz by subgrain rotation. (d) Folding of the epidote band in layer 2 and dissolution–precipitation of Epidote-B. (e) Detail of the viscous granular flow process and dynamic granular fluid pump allowing Epidote-B to precipitate in creep cavities along quartz grain boundaries. (f) Detail of quartz grain boundary sliding allowing dynamic granular fluid pump (modified from Fusseis et al., 2009). (g) Present-day microstructure. Not to scale.

3 may be linked to the closer proximity of layer 1 to the host rock, to a role of mechanically strong epidote clusters forming a load-bearing network, or to a combination of both (Handy, 1990; 1994; Masuda, 1990; 1995; Tullis, 2002; Passchier, 2005). The microstructures in layers 2–3 differing from those in layer 1 (Sect. 5.1), along with the lesser extent of chemical variability across epidote grains in layers 2–3 compared to Epidote-A in layer 1 (Figs. 10–11), suggest that the mechanism of formation

485 of Epidote-B is different than that of Epidote-A. TheThe Zener relation between quartz and epidote in layers 2–3 indicate a interplay between epidote and quartz during the formation of this microstructural domain. At the same time, the alignment of Epidote-B grains along the microfold axial planes (Figs. 4a and 6), and the presence of minute Epidote-B along grain boundaries of dynamically recrystallized quartz grains (Fig. 9) indicate9) suggest that quartz dynamic recrystallization and epidote-B formation are linked processes, thus that Epidote-B formed during deformation. The overlap in major and trace

490 element compositions of Epidote-B and Epidote-A (Figs. 10–11), though, demonstrates that these epidote generations are chemically related. One way to reconcile this geochemical affinity with different formation mechanisms is a scenario in which Epidote-B formed via deformation-induced dissolution of Epidote-A grains and (re)precipitation. during deformation. In fact, a few euhedral epidote grains can still be recognized in layer 2, (Fig. 6), which are interpreted as Epidote-A relicts inherited from the original vein morphology. The gradation from epidote-rich/quartz-poor domains to virtually epidote-free/quartz

495 dominated ones in layers 2–3 (Fig.Figs. 3, 4, 6a, 7 and 14g) suggests that the microstructure that formed upon veining was processes produced a morphology similar to that shown in Fig. 14a, and that the original vein microstructure was subsequently deformed to form the present-day epidote–quartz spatial distribution. In fact, shifts between epidote-rich and quartz-rich

Number: 1   Author: a   Subject: Sticky Note   Date: 23/09/2022 16:50:27
indicates
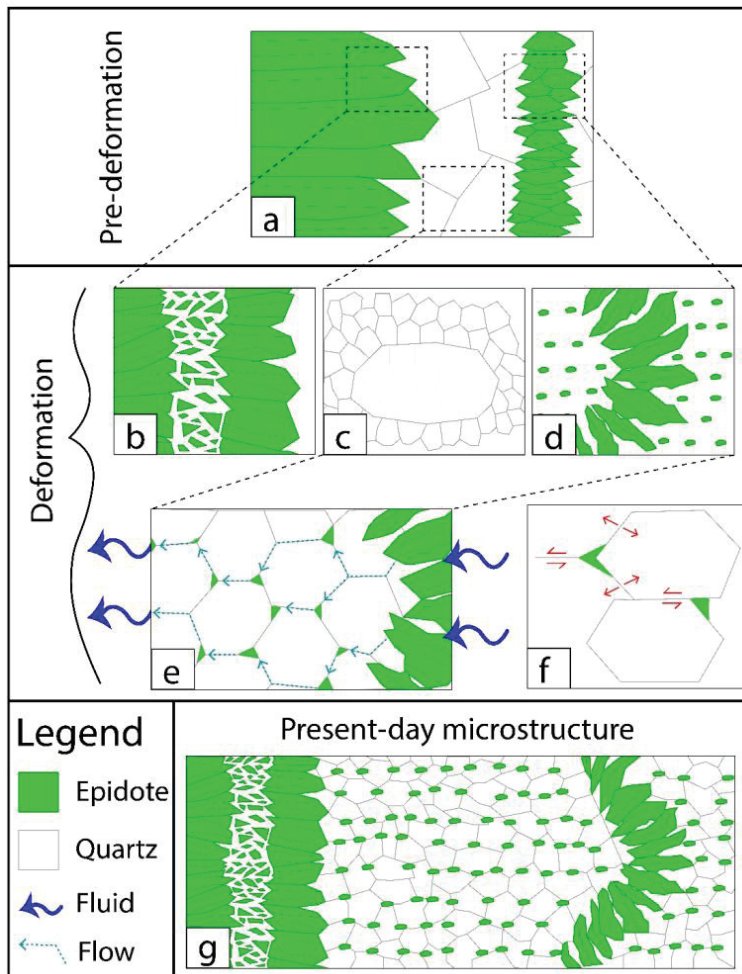
Figure 14: Sketches of the sequence of events affecting the studied epidote vein. (a) Original microstructure formed upon veining. (b) Detail of the fracturing occurring in Epidote-A in layer 1. (c) Dynamic recrystallization of quartz by subgrain rotation. (d) Folding of the epidote band in layer 2 and dissolution–precipitation forming Epidote-B. (e) Detail of the viscous granular flow process, cavitation and formation of nucleation sites ("dynamic granular fluid pump" of Fusseis et al., 2009) allowing Epidote-B to precipitate in creep cavities along quartz grain boundaries. (f) Detail of quartz grain boundary sliding allowing dynamic granular fluid pump (modified from Fusseis et al., 2009). (g) Present-day microstructure. Not to scale.

domains are frequent in epidote-quartz veins (e.g., Peverelli et al., 2021; their Figs. 1a and 1c). Further evidence for fluid-mediated mass transfer is also given by CL images of quartz (Fig. 12), which indicate that the grain boundaries of quartz interacted with an aqueous fluid. 12): these indicate trace element variability within single quartz grains, which is most likely the result of recrystallization in the presence of a fluid mediating mass-transfer processes (e.g., Ramseyer et al., 1988; Götze et al., 2001; Nègre et al., 2022). The presence of a fluid during deformation is also supported by fluid inclusions in dynamically recrystallized quartz. (Fig. 6b–c).

Number: 1   Author: a Subject: Sticky Note   Date: 23/09/2022 16:56:28
Maybe could be helpful to show Ep A with a colour and Ep 2 with another, to help the reader.

The transport of dissolved epidote-forming material towards the microfold axial planes (Fig. 14d) calls for a mechanism allowing the fluid to move throughout the deforming microstructural domain. The presence of ~~tiny~~ca. 10 µm sized Epidote-B grains along quartz grain boundaries and at triple junctions (Fig. 9) implies that dissolved epidote-forming material is

525 transported and precipitated into ~~nucleation loci. One mechanism enabling this~~locations of the new small Epidote-B sites. This is achieved by the presence of an interconnected network of porosity hosting an intergranular fluid that allows mass transfer ~~process is~~ processes. Although transport of dissolved epidote material may be possible by diffusion through an interconnected porosity network, fluid circulation at the cm scale enabling mass transfer processes is possible by cavitation with the formation of nucleation sites (Fig. 14e–f; also described as "dynamic granular fluid pump ~~(Fig. 14e–f; ";~~ see Fusseis et al., 2009; Menegon

530 et al., 2015) among sliding dynamically recrystallized quartz~~.~~ grains (Figs. 9 and 12). A first deformation step in which quartz grain size is reduced by dynamic recrystallization via subgrain rotation (Fig. 14c) is suggested by a ~~strong~~ crystallographic preferred orientation in quartz-dominated domains (Fig. 8). Once the new quartz grains are formed, grain boundary sliding produces creep cavities (Fig. ~~14f~~14e–f; see Herwegh and Jenni, 2001; Fusseis et al., 2009; Gilgannon et al., 2017; 2021), thus creating nucleation loci for Epidote-B~~.~~ (Fig. 9). A similar process is described by Gottardi and Hughes (2022) in quartzites

535 deformed at the brittle–ductile transition in the crust, in which fluid inclusions are redistributed in the quartz matrix by dynamic recrystallization of quartz by subgrain rotation and grain-boundary migration. A similar microstructure and a similar interplay of processes are also discussed ~~by Kruse and Stünitz (1999) for~~ in mafic high-temperature mylonites~~.~~ (Kruse and Stünitz, 1999) and quartzites (Nègre et al., 2021; Pongrac et al., 2022). This first step is followed by one in which the grain size and volume abundance of the newly precipitated Epidote-B grains control the grain size of quartz (Fig. 7), hence exerting control on quartz

540 deformation mechanisms by pinning the migrating quartz boundaries (see Jessel, 1987; Olgaard, 1990; Humphreys and Ardakani, 1996; Bate, 2001; Herwegh and Berger, 2004; Herwegh et al., 2011~~).~~; Cyprych et al., 2016). This ~~allows to suggest~~suggests a feedback process: (1) quartz grain boundary sliding creates creep cavities in which Epidote-B crystallizes, (2) Epidote-B keeps quartz grain size small, (3) more creep cavities are formed, and (4) more Epidote-B grains are formed. This process is referred to as viscous granular flow (e.g., Fitz Gerald and Stünitz, 1993;Stünitz and Fitz Gerald, 1993; Paterson,

545 1995; see also Kruse and Stünitz, 1999). The dissolution of epidote may have been facilitated by increased surface area achieved via brittle grain-size reduction of Epidote-A grains (Figs. 5 and 14a).

6.2 Open-system conditions and external fluids

Epidote dissolution–precipitation and the transport of dissolved epidote material to the loci of Epidote-B crystallization implies the presence of a fluid, whose nature can be assessed by Pb–Sr isotope data. We have mentioned that the epidote ~~microseparates~~micro-separates used for solution ICP-MS measurements mix Epidote-A and Epidote-B to unknown proportions, since the mechanical separation of pure Epidote-B is not feasible due to its small grain size. ~~The~~Therefore, the observation that ^{238}~~U/^{206}Pb and~~ the ^{207}Pb/^{206}Pb ~~ratios of the microseparates do not lie on the same regression as those measured by LA-ICP-MS in Epidote-A~~ and ^{87}Sr/^{86}Sr ratios of the micro-separates are different (Fig. ~~13a~~13) suggests that the ~~epidote microseparates~~micro-separates include different epidote ~~generation, thus~~generations, hence that Epidote-A and Epidote-B crystallized from fluids with different Pb and Sr isotope compositions. This is supported by the ~~^{87}Sr/^{86}Sr~~Pb–Sr isotopic ratios of the ~~microseparates~~micro-separates being different than that measured in an Epidote-A grain (Fig. ~~13b~~13; Table 2). There are two principal processes that can induce changes in the Pb and Sr isotope compositions: (1) radioactive decay of ^{235,238}U into ^{207,206}Pb and ^{87}Rb into ^{87}Sr, or (2) open-system conditions allowing for advection of extraneous Pb and Sr with different isotopic compositions. Process (1) is unlikely in this case because ingrown radiogenic Pb and Sr ~~of such young epidote are negligible.~~would not be sufficient to cause the observed differences among micro-separates and Epidote-A grain (Fig. 13). Consequently, the ~~U–~~Pb–Sr isotope heterogeneity of the two epidote generations infers fluid-mediated addition of extraneous Sr and Pb during crystallization of Epidote-B. Because the vein microstructure carries evidence of a single deformation event (Fig. 14g), it is likely that a second fluid type entered the system during vein deformation and formation of Epidote-B (Fig. 14e–f). Thus, the differences in ~~U–~~Pb and Sr isotopic data ~~between LA-ICP-MS~~of Epidote-A grain and ~~solution ICP-MS/TIMS data~~micro-separates are interpreted to document mixing between different contributions: (1) one reflecting the isotopic composition of Epidote-A incorporated upon vein formation, and (2) one reflecting the mixing of dissolved Epidote-A material with extraneous Pb and Sr brought to the site of Epidote-B crystallization. The existence of open-system conditions bears the potential for fluid-mediated transfer of chemical constituents (Figs. 14e–f). The fact that the major and trace element chemical composition of Epidote-B ~~is identical to, and less variable than~~maintains the same patterns as, and represents a narrower range of, that of Epidote-A (Figs. 10–11) suggests similarly (either rock- or fluid-) buffered conditions. Hence, during fluid-mediated crystallization of Epidote-A and Epidote-B ~~at closely comparable,~~ physico-chemical (e.g., P, T, fO$_2$) conditions ~~and~~ thus fluid

compositioncompositions – were closely comparable. The initial compositional variability of Epidote-A got thereby homogenized upon dissolution and crystallization into Epidote-B. Considering that the 299 ± 2 Ma old host granitoid (Schaltegger and Corfu, 1992; Ruiz et al., 2022) contains minerals with high concentrations of U, Th and Rb (e.g., allanite, biotite), even slightly variable contributions of radiogenic Pb and Sr leached from these minerals may produce a measurable shift in Pb–Sr isotope ratios without a resolvable effect on Sr and Pb fluid concentrations. Also, crystallization of Epidote-A and Epidote-B most likely occurred at comparable T conditions (ca. 400–450 °C as inferred from the presence of biotite in the vein; see Goncalves et al., 2012). Hence, fluid/epidote partition coefficients of all measured elements remained similar between the two epidote crystallization events. Such a scenario can well account for the compositional uniformity but Pb and Sr isotopic heterogeneitydifferences between Epidote-A and Epidote-B, hence allowing that at least a fraction of the fluid involved in the deformation of layers 2–3 is of external origin. Peverelli et al. (accepted2022) measured the H isotope composition of epidote in this sample, obtaining values that can only be explained as a mixture of end-member waters (e.g., meteoric, seawater, etc.) as source for the epidote-forming fluids. In light of the present data, it is possible that their measured δD value reflects the mixing of internal and external fluids upon deformation of the epidote-quartz vein as described above.

6.3 Epidote geochemistry as a result of veining vs. ~~granular fluid pump~~combined grain boundary sliding, cavitation, and nucleation

The present major and trace element data show that Epidote-B is geochemically similar to, and less variable than, Epidote-A (Figs. 10–11), and this result ~~bears important implications on epidote~~ might be linked to differences in crystallization mechanisms~~.~~ between the two epidote generations. In a rock-dominated system, the larger geochemical variability of Epidote-A may be due to (1) fluid distillation during epidote crystallization, (2) slight variations in physico-chemical conditions (e.g., P, T) throughout the veining processes, or (3) pulsating fluid fluxes ~~(i.e., multiple Epidote-A generations). The latter is unlikely because all laser spots for U–Pb dating define one statistically robust regression with MSWD of 0.79, providing no evidence for multiple epidote generations at the current analytical precision. Such a hypothesis is also inconsistent with trace~~. Trace element data (Fig. 11a–b) defining trends and not distinct epidote populations~~. These observations~~ suggest that the geochemical variability of Epidote-A is ~~due to~~most readily explained by an evolving epidote-forming fluid chemistry along with more and more epidote precipitating, thus readily removing compatible elements from the fluid (see also Anenburg et al., 2015). This

does not exclude multiple pulses of the same fluid (i.e., same fluid source and chemistry) and a role for varying physico-chemical conditions, such a small temperature variations (e.g., Trincal et al., 2015). The lesser extent of chemical variation in Epidote-B indicates homogenization of the whole trace element budget dissolved into the Epidote-B-forming fluid. Viscous granular flow is a dynamic process in which continuous feedback exists among dissolution of minerals, grain boundary sliding, creep cavitation, mass transfer and mineral precipitation (e.g., Fitz Gerald and Stünitz, 1993; Stünitz and Fitz Gerald, 1993; Paterson, 1995). This implies that repeated dissolution and reprecipitation of the same material is likely to occur, and the chemical budget gets compositionally homogenized with ongoing deformation. Consequently, in the case of the epidote-quartz microfold in layers 2–3, such a mechanism may account for the chemical homogeneity of Epidote-B. If this respect, ~~granular fluid pump promotes~~combined grain boundary sliding, cavitation, and nucleation promote recycling and homogenization of fluids in deforming polymineralic aggregates.

7 Consequences for epidote U–Pb ages

The inevitable question arising from the scenario developed above is what ~~is the significance of~~ the U–Pb age measured in Epidote-A reflects. Temperature-driven resetting of the U–Pb system is excluded based on the peak temperature reached in the area (i.e~~.~~, 450 ± 30 °C; Challandes et al., 2008; Goncalves et al., 2012) never exceeding the closure temperature for Pb diffusion in epidote (i.e~~.~~, > 685 °C; Dahl, 1997). As a consequence, ~~diffusional processes do~~solid-volume diffusion does not have the potential to affect Epidote-A U–Pb ages. However, the ~~disturbance of the~~ U–Pb isotope system may be affected by dissolution–precipitation ~~mechanisms~~, as has been reported for many minerals (e.g., monazite; Tartèse et al., 2011; Williams et al., 2011; Seydoux-Guillaume et al., 2012; Grand'Homme et al., 2018). Fluid–rock interaction has been shown to affect other isotopic systems as well (e.g., K–Ar, B; Halama et al., 2014). The microstructural relationships between Epidote-A and biotite in layer 1 are consistent with both minerals forming together in Alpine times and before vein deformation. ~~Also, the~~The U–Pb isotopic data presented in Peverelli et al. (2021) resolve a single generation of Epidote-A ~~when plotted~~at the available analytical precision in a Tera–Wasserburg diagram~~. Moreover, the time-resolved~~, which plots $^{238}U/^{206}Pb$~~$/^{238}U$~~ vs. $^{207}Pb/^{206}Pb$ ratios ~~corrected for downhole fractionation display flat trends~~ when corrected for zoning in initial lead by applying a ^{208}Pb correction ~~(see Fig. (Tera~~5 of Peverelli et al., 2021). This means that there is no resolvable isotopic zoning across the ca. 10–

26

12 μm crater depth of the LA-ICP-MS measurements. The trace element data (Figs. 10c and 11; Table 2) reveal prominent chemical zoning.Wasserburg, 1972). If any isotopic heterogeneity had been caused by interaction with the deformation-related fluid, the crystal rims would be affected to a greater extent than the cores. Consequently, if resolvable isotopic zoning existed in the dated Epidote-A grains, plotting data-points from different domains of isotopic zoning would create scatter of the data-points in a Tera–Wasserburg diagram. However, U–Pb isotope measurements cover all geochemicallychemically variable zones in Epidote-A (Fig. 10; white circles) and they define a single Tera–Wasserburg regression regardless of their proximity to cores/rims of the analyzed epidote grains. Moreover, the time-resolved $^{206}Pb/^{238}U$ ratios corrected for downhole fractionation display flat trends when corrected for zoning in initial Pb by applying a ^{208}Pb correction (see Fig. 5 of Peverelli et al., 2021). This means that there is no resolvable isotopic zoning across the ca. 10–12 μm crater depth of the LA-ICP-MS measurements. Finally, the trace element data (Figs. 10c and 11; Table 2) reveal preserved prominent chemical zoning. This supports that the dissolution–precipitation processes during Epidote-B formation did not appreciably disturb the U–Pb isotope system in Epidote-A relicts to a noticeable extent at the available analytical precision.


8 Conclusions and outlook

This study combines microstructural and geochemical methods to investigate the formation mechanisms of an epidote-quartz microfold within an epidote-quartz (±biotite) vein. For the first time, weWe have demonstratedsuggested the occurrence of epidote dissolution–precipitation processes, and that this mechanism coexists with quartz dynamic recrystallization, both contributing to grain-size reduction of the system. The genetic link between epidote grains being dissolved and those being reprecipitated is revealed by the overlap of the major and trace element compositions of both generations. We have shown that fluid circulation at the scale of the thin section and the formation of epidote nucleation loci in the deforming system are enabled by dynamic granular fluid pumpa combination of grain boundary sliding, creep cavitation, and mass transfer. Repeated dissolution and (re)precipitation processes of epidote in creep cavities formed among sliding quartz grainsgrain boundaries also cause chemical homogenization of the epidote-dissolving/forming fluid, and hence of the new epidote generation forming during deformation. This demonstrates the importance of fluid recycling in deformational processes, although the application of Pb–Sr isotope geochemistry recognizes a role for the addition of externally derived fluids mediating mass transfer processes

645   in the studied epidote-quartz vein. Epidote plays an active role in determining the deformation behavior of other minerals, hence in the deformation style of polymineralic aggregates and in producing the resulting microstructures. To our knowledge, before this study, only brittle deformation behavior of epidote had been proven (Masuda et al., 1990; 1995), but no other detailed studies had addressed epidote deformation mechanisms. In this respect, although Stünitz and Fitz Gerald (1993) do not observe any plastic deformation in clinozoisite, epidote dynamic recrystallization has never been either ruled out or

650   demonstrated rigorously. However, since this mineral is widespread in crustal rocks (e.g., Bird and Spieler, 2004; Enami et al., 2004; Franz and Liebscher, 2004; Grapes and Hoskin, 2004; Schmidt and Poli, 2004; Morad et al., 2010), the occurrence of epidote ductile deformation may have effects on the deformation of the continental crust and it calls for a better understanding of this mineral.

Appendix A

Transmitted light microscope images of the other epidote-quartz veins (samples P2, P3 and Gr0-c) associated with the studied epidote-quartz vein.
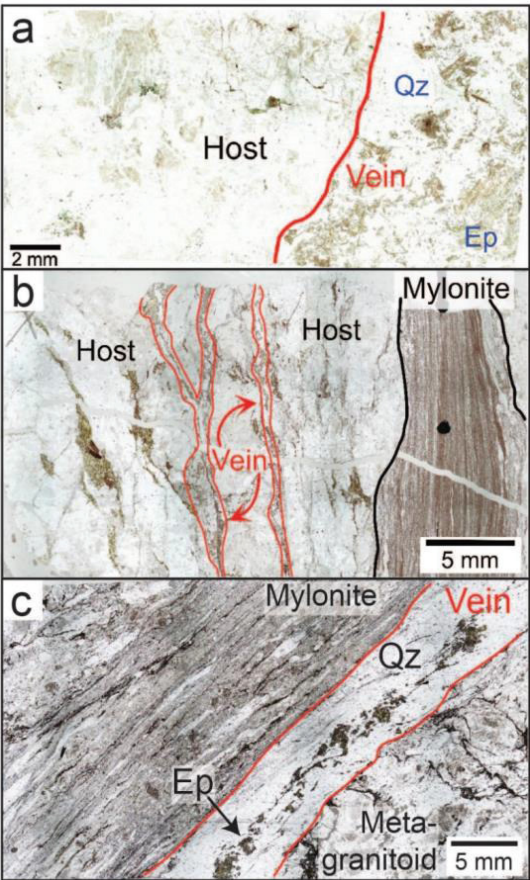
Figure A1: Transmitted light scans of (a) epidote vein P2, (b) epidote vein P3 and (c) epidote vein Gr0-c. Plane-polarized light.
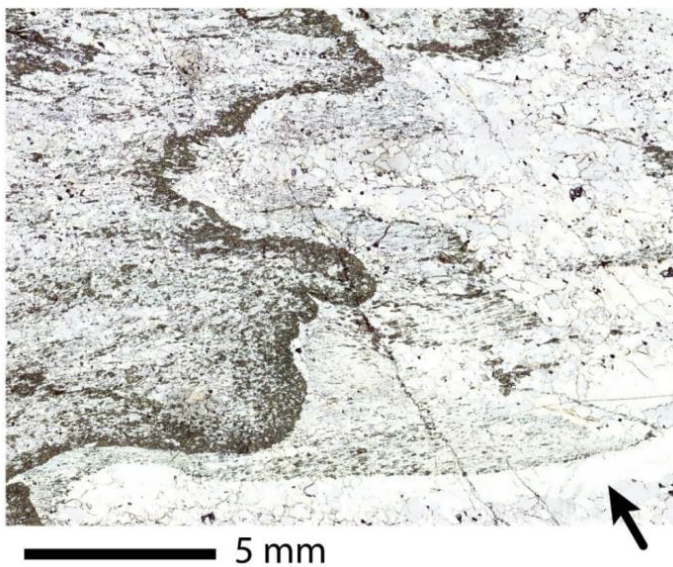
5 mm

Appendix B

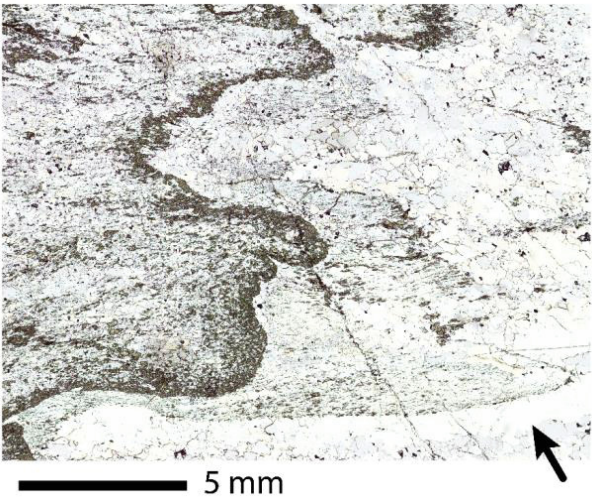Transmitted light photograph of the microfold in layers 2–3.

680

5 mm

Figure A1: Transmitted light scan of layers 2–3. Plane-polarized light.

Figure C1: Electron backscatter diffraction (EBSD) map showing the orientation of quartz C axis in layer

700

Formatted: Line spacing: 1.5 lines

Author contribution

705 VP prepared the samples, carried out grain-size analysis and petrographic description, planned electron microprobe work, ran trace element measurements by LA-ICP-MS, measured Sr isotopes by TIMS, and prepared the manuscript. AB and MH supervised the work and greatly contributed to structuring the manuscript. MW supervised clean lab work and TIMS analyses, and measured Pb isotope data with IMV. TP granted access to the LA-ICP-MS laboratory and was closely involved in structuring the manuscript and in data evaluation. PL performed work at the electron microprobe and processed the X-ray

710 maps. All authors read the manuscript and contributed to its improvement.

Competing interests

The authors declare that they have no conflict of interest.

Code/data availability

All data are included in the manuscript (see tables).

31

725 **References**

Anenburg, M., Katzir, Y., Rhede, D., Jöns, N., and Bach, W.: Rare earth element evolution and migration in plagiogranites: a record preserved in epidote and allanite of the Troodos ophiolite, Contrib. to Mineral. Petrol., 169, https://doi.org/10.1007/s00410-015-1114-y, 2015.

Bambauer, H. U., Herwegh, M., and Kroll, H.: Quartz as indicator mineral in the Central Swiss Alps: The quartz
730 recrystallization isograd in the rock series of the northern Aar massif, Swiss J. Geosci., 102, 345–351, https://doi.org/10.1007/s00015-009-1319-z, 2009.

Barth, S., Oberli, F., Meier, M.: Th–Pb versus U–Pb isotope systematics in allanite from co-genetic rhyolite and granodiorite: implications for geochronology. Earth Planet. Sci. Lett. ~~124, 149–159, https://doi.org/10.1016/0012-821X(94)00073-5,~~124, 149–159, https://doi.org/10.1016/0012-821X(94)00073-5, 1994.

735 Bate, P.: The effect of deformation on grain growth in Zener pinned systems. Acta Mater. 49, 1453–1461, https://doi.org/10.1016/S1359-6454(01)00033-7, 2001.

Belgrano, T. M., Herwegh, M., and Berger, A.: Inherited structural controls on fault geometry, architecture and hydrothermal activity: an example from Grimsel Pass, Switzerland, Swiss J. Geosci., 109, 345–364, https://doi.org/10.1007/s00015-016-0212-9, 2016.

740 Bergemann, C., Gnos, E., Berger, A., Whitehouse, M., Mullis, J., Wehrens, P., Pettke, T., Janots, E.: Th-Pb ion probe dating of zoned hydrothermal monazite and its implications for repeated shear zone activity: An example from the central alps, Switzerland. Tectonics 36, 671–689, ~~https://doi.org/10.1002/2016TC004407,~~https://doi.org/10.1002/2016TC004407, 2017.

Berger, A., Gnos, E., Janots, E., Whitehouse, M., Soom, M., Frei, R., Waight, T.E.: Dating brittle tectonic movements with cleft monazite: Fluid-rock interaction and formation of REE minerals. Tectonics 32, 1176–1189,
745 ~~https://doi.org/10.1002/tect.20071,~~https://doi.org/10.1002/tect.20071, 2013.

Berger, A., Mercolli, I., Herwegh, M., Gnos, E.: Geological Map of the Aar Massif, Tavetsch and Gotthard Nappes. Geol. spec. Map 1:100 000, explanatory notes 129. Federal Office of Topogaphy swisstopo, Bern, Switzerland, 2017

Berger, A., Wehrens, P., Lanari, P., Zwingmann, H., Herwegh, M.: Microstructures, mineral chemistry and geochronology of white micas along a retrograde evolution: An example from the Aar massif (Central Alps, Switzerland). Tectonophysics 721,
750 179–195, ~~https://doi.org/10.1016/j.tecto.2017.09.019,~~https://doi.org/10.1016/j.tecto.2017.09.019, 2017.

Berger, A., Egli, D., Glotzbach, C., Valla, P.G., Pettke, T., Herwegh, M.: Apatite low-temperature chronometry and microstructures across a hydrothermally active fault zone. Chem. Geol. ~~588, 120633, https://doi.org/10.1016/j.chemgeo.2021.120633,~~588, 120633, https://doi.org/10.1016/j.chemgeo.2021.120633, 2022.

Bird, D. K. and Spieler, A. R.: Epidote in Geothermal Systems, Rev. Mineral. Geochemistry 56, 235–300,
755 ~~https://doi.org/10.2138/gsrmg.56.1.235,~~https://doi.org/10.2138/gsrmg.56.1.235, 2004.

Bons, P.D., Elburg, M.A., Gomez-Rivas, E.: A review of the formation of tectonic veins and their microstructures. J. Struct. Geol. ~~43, 33–62, https://doi.org/10.1016/j.jsg.2012.07.005,~~43, 33–62, https://doi.org/10.1016/j.jsg.2012.07.005, 2012.

32

Bukovská, Z., Jeřábek, P., Morales, F.G.: Major softening at brittle-ductile transition due to interplay between chemical and deformation processes: An insight from evolution of shear bands in the South Armorican Shear Zone. J. Geophys. Res. Solid Earth 1158–1182. https://doi.org/10.1002/2015JB012319, 2016

Challandes, N., Marquer, D., Villa, I.M.: P-T-t modelling, fluid circulation, and 39Ar-40Ar and Rb-Sr mica ages in the Aar Massif shear zones (Swiss Alps). Swiss J. Geosci. ~~101, 269–288, https://doi.org/10.1007/s00015-008-1260-6,~~101, 269–288, https://doi.org/10.1007/s00015-008-1260-6, 2008.

Choukroune, P. and Gapais, D.: Strain pattern in the Aar Granite (Central Alps): orthogneiss developed by bulk inhomogeneous flattening, 5, 411–418, https://doi.org/10.1016/b978-0-08-030273-7.50019-7, 1983.

Cyprych, D., Piazolo, S., Wilson, C.J.L., Luzin, V., Prior, D.J.: Rheology, microstructure and crystallographic preferred orientation of matrix containing a dispersed second phase: Insight from experimentally deformed ice. Earth Planet. Sci. Lett. 449, 272–281, https://doi.org/10.1016/j.epsl.2016.06.010, 2016.

Dahl, P. S.: A crystal-chemical basis for Pb retention and fission-track annealing systematics in U-bearing mineral, with implications for geochronology, Earth Planet. Sci. Lett., 150, 277–290, ~~https://doi.org/10.1016/S0012-821X(97)00108-8,~~https://doi.org/10.1016/S0012-821X(97)00108-8, 1997.

Diamond, L. W., Wanner, C., and Waber, H. N.: Penetration depth of meteoric water in orogenic geothermal systems, Geology, 46, 1083–1066, https://doi.org/10.1130/G45394.1, 2018.

Egli, D., Baumann, R., Küng, S., Berger, A., Baron, L., and Herwegh, M.: Structural characteristics, bulk porosity and evolution of an exhumed long-lived hydrothermal system, 747–748, 239–258, https://doi.org/10.1016/j.tecto.2018.10.008, 2018.

Enami, M., Liou, J.G., Mattinson, C.G.: Epidote minerals in high P/T metamorphic terranes: Subduction zone and high- to ultrahigh-pressure metamorphism. Rev. Mineral. Geochemistry 56, 347–398, ~~https://doi.org/10.2138/gsrmg.56.1.347,~~https://doi.org/10.2138/gsrmg.56.1.347, 2004.

Evans, B., Renner, J., and Hirth, G.: A few remarks on the kinetics of static grain growth in rocks, 90, 88–103, https://doi.org/10.1007/s005310000150, 2001.

Feineman, M. D., Ryerson, F. J., DePaolo, D. J., and Plank, T.: Zoisite-aqueous fluid trace element partitioning with implications for subduction zone fluid composition, 239, 250–265, https://doi.org/10.1016/j.chemgeo.2007.01.008, 2007.

Ferreira, T., Rasband, W.: ImageJ User Guide User Guide ImageJ. Image J user Guid. 1.46r. ~~https://doi.org/10.1038/nmeth.2019,~~https://doi.org/10.1038/nmeth.2019, 2012.

Fitz Gerald, J.D., Stünitz, H.: Deformation of granitoids at low metamorphic grade. I: Reactions and grain size reduction. Tectonophysics 221, 269–297, ~~https://doi.org/10.1016/0040-1951(93)90163-E,~~https://doi.org/10.1016/0040-1951(93)90163-E, 1993.

Franz, G., Liebscher, A.: Physical and Chemical Properties of the Epidote Minerals-An Introduction-. Rev. Mineral. Geochemistry 56, 1–81, ~~https://doi.org/10.2138/gsrmg.56.1.1,~~https://doi.org/10.2138/gsrmg.56.1.1, 2004.

33

Frei, D., Liebscher, A., Franz, G., Dulski, P.: Trace element geochemistry of epidote minerals. Rev. Mineral. Geochemistry 56, 553–605, https://doi.org/10.2138/gsrmg.56.1.553,https://doi.org/10.2138/gsrmg.56.1.553, 2004.

Gieré, R., Sorensen, S.S.: Allanite and other REE-rich epidote-group minerals. Rev. Mineral. Geochemistry 56, 431–493, https://doi.org/10.2138/gsrmg.56.1.431,https://doi.org/10.2138/gsrmg.56.1.431, 2004.

795 Gilgannon, J., Fusseis, F., Menegon, L., Regenauer-Lieb, K., and Buckman, J.: Hierarchical creep cavity formation in an ultramylonite and implications for phase mixing, 8, 1193–1209, https://doi.org/10.5194/se-8-1193-2017, 2017.

Gilgannon, J., Waldvogel, M., Poulet, T., Fusseis, F., Berger, A., Barnhoorn, A., and Herwegh, M.: Experimental evidence that viscous shear zones generate periodic pore sheets, 12, 405–420, https://doi.org/10.5194/se-12-405-2021, 2021.

Giuntoli, F., Menegon, L., Warren, C.J.: Replacement reactions and deformation by dissolution and precipitation processes in 800 amphibolites. J. Metamorph. Geol. 36, 1263–1286, https://doi.org/10.1111/jmg.12445, 2018.

Goncalves, P., Oliot, E., Marquer, D., Connolly, J.A.D.: Role of chemical processes on shear zone formation: An example from the Grimsel metagranodiorite (Aar massif, Central Alps). J. Metamorph. Geol. 30, 703–722, https://doi.org/10.1111/j.1525-1314.2012.00991.x,30, 703–722, https://doi.org/10.1111/j.1525-1314.2012.00991.x, 2012.

Gottardi, R., Hughes, B.: Role of fluids on deformation in mid-crustal shear zones, Raft River Mountains, Utah. Geol. 805 Magazine, 1 – 13, doi:10.1017/S0016756822000231, 2022.

Götze, J., Plötze, M., Habermann, D.: Origin, spectral characteristics and practical applications of the cathodoluminescence (CL) of quartz - A review. Mineral. Petrol. 71, 225–250, https://doi.org/10.1007/s007100170040, 2001.

Grand'Homme, A., Janots, E., Seydoux-Guillaume, A.M., Guillaume, D., Magnin, V., Hövelmann, J., Höschen, C., Boiron, M.C.: Mass transport and fractionation during monazite alteration by anisotropic replacement. Chem. Geol. 484, 51–68, 810 https://doi.org/10.1016/j.chemgeo.2017.10.008,484, 51–68, https://doi.org/10.1016/j.chemgeo.2017.10.008, 2018.

Grapes, R.H., Hoskin, P.W.O.: Epidote group minerals in low-medium pressure metamorphic terranes. Rev. Mineral. Geochemistry 56, 301–345, https://doi.org/10.2138/gsrmg.56.1.301,https://doi.org/10.2138/gsrmg.56.1.301, 2004.

Guillong, M., Meier, D.L., Allan, M.M., Heinrich, C.A., Yardley, B.W.D., 2008. SILLS: A Matlab-Based Program for the Reduction of Laser Ablation ICP–MS Data of Homogeneous Materials and Inclusions. Mineral. Assoc. Canada Short Course 815 40, 328–333.

Haeusler M., Haas C., Lösch S., Moghaddam N., Villa I.M., Walsh S., Kayser M., Seiler R., Ruehli F., Janosa M., Papageorgopoulou C.: Multidisciplinary identification of the controversial freedom fighter Jörg Jenatsch, assassinated 1639 in Chur, Switzerland. PLOS ONE, 11(12): e0168014, 1-22, doi: 10.1371/journal.pone.0168014, 2016.

Halama, R., Konrad-Schmolke, M., Sudo, M., Marschall, H.R., Wiedenbeck, M.: Effects of fluid-rock interaction on 820 40Ar/39Ar geochronology in high-pressure rocks (Sesia-Lanzo Zone, Western Alps). Geochim. Cosmochim. Acta 126, 475–494, https://doi.org/10.1016/j.gca.2013.10.023,https://doi.org/10.1016/j.gca.2013.10.023, 2014.

Halter, W.E., Pettke, T., Heinrich, C.A., Rothen-Rutishauser, B.: Major to trace element analysis of melt inclusions by laser-ablation ICP-MS: Methods of quantification. Chem. Geol. 183, 63–86, https://doi.org/10.1016/S0009-2541(01)00372-2,183, 63–86, https://doi.org/10.1016/S0009-2541(01)00372-2, 2002.

34

825   Handy, M. R.: The solid-state flow of polymineralic rocks, J. Geophys. Res.-Earth, 95, 8647–8661, https://doi.org/10.1029/JB095iB06p08647, 1990.

Handy, M. R.: Flow laws for rocks containing two non-linear viscous phases: A phenomenological approach, J. Struct. Geol., 16, 287–301, https://doi.org/10.1016/0191-8141(94)90035-3, 1994.

Hentschel, F., Janots, E., Trepmann, C.A., Magnin, V., Lanari, P., 2020. Corona formation around monazite and xenotime
830   during greenschist-facies metamorphism and deformation. Eur. J. Mineral. 32, 521–544. https://doi.org/10.5194/ejm-32-521-2020

Herwegh, M., & Berger, A.: Deformation mechanisms in second-phase affected microstructures and their energy balance. Journal of Structural Geology, 26(8), 1483–1498, https://doi.org/10.1016/j.jsg.2003.10.006,https://doi.org/10.1016/j.jsg.2003.10.006, 2004.

835   Herwegh, M. and Jenni, A.: Granular flow in polymineralic rocks bearing sheet silicates: New evidence from natural examples, 332, 309–320, https://doi.org/10.1016/S0040-1951(00)00288-2, 2001.

Herwegh, M., Linckens, J., Ebert, A., Berger, A., Brodhag, S.H.: The role of second phases for controlling microstructural evolution in polymineralic rocks: A review. J. Struct. Geol. 33, 1728–1750, https://doi.org/10.1016/j.jsg.2011.08.011,33, 1728–1750, https://doi.org/10.1016/j.jsg.2011.08.011, 2011.

840   Herwegh, M., Berger, A., Baumberger, R., Wehrens, P., Kissling, E.: Large-Scale Crustal-Block-Extrusion During Late Alpine Collision. Sci. Rep. 7, 1–10, https://doi.org/10.1038/s41598-017-00440-0,7, 1–10, https://doi.org/10.1038/s41598-017-00440-0, 2017.

Herwegh, M., Berger, A., Glotzbach, C., Wangenheim, C., Mock, S., Wehrens, P., Baumberger, R., Egli, D., and Kissling, E.: Late stages of continent-continent collision: Timing, kinematic evolution, and exhumation of the Northern rim (Aar Massif)
845   of the Alps, Earth-Science Rev., 200, 102959, https://doi.org/10.1016/j.earscirev.2019.102959, 2020.

Hobbs, B.E., Ord, A., Spalla, M.I., Gosso, G., Zucali, M.: The interaction of deformation and metamorphic reactions. Geol. Soc. Spec. Publ. 332, 189–223, https://doi.org/10.1144/SP332.12,https://doi.org/10.1144/SP332.12, 2010.

Hofmann, B. A., Helfer, M., Diamond, L. W., Villa, I. M., Frei, R., and Eikenberg, J.: Topography-driven hydrothermal breccia mineralization of Pliocene age at Grimsel Pass, Aar massif, Central Swiss Alps, Schweizerische Mineral. und Petrogr.
850   Mitteilungen, 84, 271–302, 2004.

Horwitz, E. P., Dietz, M. L., and Chiarizia, R.: The application of novel extraction chromatographic materials to the characterization of radioactive waste solutions, J. Radioanal. Nucl. Ch., 161, 575–583, https://doi.org/10.1007/bf02040504,https://doi.org/10.1007/bf02040504, 1992.

Humphreys, F.J., Ardakani, M.G.: Grain boundary migration and zener pinning in particle-containing copper crystals. Acta
855   Mater. 44, 2717–2727, https://doi.org/10.1016/1359-6454(95)00421-1, 1996.

Janots, E., Berger, A., Gnos, E., Whitehouse, M., Lewin, E., Pettke, T.: Constraints on fluid evolution during metamorphism from U-Th-Pb systematics in Alpine hydrothermal monazite. Chem. Geol. 326–327, 61–71, https://doi.org/10.1016/j.chemgeo.2012.07.014,326–327, 61–71, https://doi.org/10.1016/j.chemgeo.2012.07.014, 2012.

35

Jessell, M.W.: Grain-boundary migration microstructures in a naturally deformed quartzite. J. Struct. Geol. 9, 1007–1014, https://doi.org/10.1016/0191-8141(87)90008-3, 1987.

Karato, S.-I.: Deformation of Earth Materials: An Introduction to the Rheology of Solid Earth, Cambridge University Press, https://doi.org/10.1007/s00024-009-0536-8, 2009.

Kruse, R., Stünitz, H.: Deformation mechanisms and phase distribution in mafic high-temperature mylonites from the Jotun Nappe, southern Norway. Tectonophysics 303, 223–249, https://doi.org/10.1016/S0040-1951(98)00255-8,https://doi.org/10.1016/S0040-1951(98)00255-8, 1999.

Konrad-Schmolke, M., Halama, R., Wirth, R., Thomen, A., Klitscher, N., Morales, L., Schreiber, A., Wilke, F.D.H.: Mineral dissolution and reprecipitation mediated by an amorphous phase. Nat. Commun. 9, https://doi.org/10.1038/s41467-018-03944-z,9, https://doi.org/10.1038/s41467-018-03944-z, 2018.

Lanari, P., Duesterhoeft, E.: Modeling Metamorphic Rocks Using Equilibrium Thermodynamics and Internally Consistent Databases: Past Achievements, Problems and Perspectives. J. Petrol. 60, 19–56, https://doi.org/10.1093/petrology/egy105,60, 19–56, https://doi.org/10.1093/petrology/egy105, 2019.

Lanari, P., Vidal, O., De Andrade, V., Dubacq, B., Lewin, E., Grosch, E.G., Schwartz, S.: XMapTools: A MATLAB©-based program for electron microprobe X-ray image processing and geothermobarometry. Comput. Geosci. 62, 227–240, https://doi.org/10.1016/j.cageo.2013.08.010,62, 227–240, https://doi.org/10.1016/j.cageo.2013.08.010, 2014.

Lanari, P., Vho, A., Bovay, T., Airaghi, L., Centrella, S.: Quantitative compositional mapping of mineral phases by electron probe micro-analyser. Geol. Soc. Spec. Publ. 478, 39–63, https://doi.org/10.1144/SP478.4,478, 39–63, https://doi.org/10.1144/SP478.4, 2019.

Ludwig, K. R., 2012: On the treatment of concordant uranium-lead ages, Geochim. Cosmochim. Ac., 62, 665–676, https://doi.org/10.1016/S0016-7037(98)00059-3, 1998.

Marquer, D. and Burkhard, M.: Fluid circulation, progressive deformation and mass-transfer processes in the upper crust: the example of basement – cover relationships in the External Crystalline Massifs, Switzerland, J. Struct. Geol., 8–9, 1047–1057, 1992.

Marquer, D. and Peucat, J. J.: Rb-Sr systematics of recrystallized shear zones at the greenschist- amphibolite transition: examples from granites in the Swiss central Alps, 74, 343–358, 1994.

Masuda, T., Shibutani, T., Kuriyama, M., Igarashi, T.: Development of microboudinage: an estimate of changing differential stress with increasing strain. Tectonophysics 178, 379–387, https://doi.org/10.1016/0040-1951(90)90160-A,https://doi.org/10.1016/0040-1951(90)90160-A, 1990.

Masuda, T., Shibutani, T., Yamaguchi, H.: Comparative rheological behaviour of albite and quartz in siliceous schists revealed by the microboudinage of piedmontite. J. Struct. Geol. 17, 1523–1533, https://doi.org/10.1016/0191-8141(95)00060-Q,17, 1523–1533, https://doi.org/10.1016/0191-8141(95)00060-Q, 1995.

McClay, K. R.: Pressure solution and Coble creep in rocks and minerals: A review, J. Geol. Soc. London., 134, 57–70, https://doi.org/10.1144/gsjgs.134.1.0057, 1977.

McDonough, W.F., Sun, S.S.: The composition of the Earth. Chem. Geol. ~~120, 223–253, https://doi.org/10.1016/0009-2541(94)00140-4,~~120, 223–253, https://doi.org/10.1016/0009-2541(94)00140-4, 1995.

895 Menegon, L., Fusseis, F., Stünitz, H., Xiao, X.: Creep cavitation bands control porosity and fluid flow in lower crustal shear zones. Geology 43, 227–230, https://doi.org/10.1130/G36307.1, 2015.

Morad, S., El-Ghali, M.A.K., Caja, M.A., Sirat, M., Al-Ramadan, K., Manurberg, H.: Hydrothermal alteration of plagioclase in granitic rocks from Proterozoic basement of SE Sweden. Geol. J. 45, 105–116, ~~https://doi.org/10.1002/gj.1178,~~https://doi.org/10.1002/gj.1178, 2010.

900 Mullis, J., Dubessy, J., Poty, B., O'Neil, J.: Fluid regimes during late stages of a continental collision: Physical, chemical, and stable isotope measurements of fluid inclusions in fissure quartz from a geotraverse through the Central Alps, Switzerland. Geochim. Cosmochim. Acta 58, 2239–2267, ~~https://doi.org/10.1016/0016-7037(94)90008-6,~~https://doi.org/10.1016/0016-7037(94)90008-6, 1994.

Nègre, L., Stünitz, H., Raimbourg, H., Lee, A., Précigout, J., Pongrac, P., Jeřábek, P.: Effect of pressure on the deformation of

905 quartz aggregates in the presence of H2O. J. Struct. Geol. 148. https://doi.org/10.1016/j.jsg.2021.104351, 2021.

Oliver, N.H.S., Bons, P.D.: Mechanisms of fluid flow and fluid-rock interaction in fossil metamorphic hydrothermal systems inferred from vein-wall rock patterns, geometry and microstructure. Geofluids 1, 137–162, https://doi.org/10.1046/j.1468-8123.2001.00013.x, 2001.

Passchier, C.W. and Trouw, R.A.: Microtectonics. Springer Science & Business Media, 2005.

910 Paterson, M. S.: A theory for granular flow accommodated by material transfer via an intergranular fluid, 245, 135–151, https://doi.org/10.1016/0040-1951(94)00231-W, 1995.

Pearce, M.A., Timms, N.E., Hough, R.M., Cleverley, J.S.: Reaction mechanism for the replacement of calcite by dolomite and siderite: Implications for geochemistry, microstructure and porosity evolution during hydrothermal mineralisation. Contrib. to Mineral. Petrol. 166, 995–1009, https://doi.org/10.1007/s00410-013-0905-2, 2013.

915 Pettke, T., Oberli, F., Audétat, A., Guillong, M., Simon, A.C., Hanley, J.J., Klemm, L.M.: Recent developments in element concentration and isotope ratio analysis of individual fluid inclusions by laser ablation single and multiple collector ICP-MS. Ore Geol. Rev. ~~44, 10–38, https://doi.org/10.1016/j.oregeorev.2011.11.001,~~44, 10–38, https://doi.org/10.1016/j.oregeorev.2011.11.001, 2012.

Peverelli, V., Ewing, T., Rubatto, D., Wille, M., Berger, A., Villa, I.M., Lanari, P., Pettke, T., Herwegh, M.: U–Pb

920 geochronology of epidote by laser ablation inductively coupled plasma mass spectrometry (LA-ICP-MS) as a tool for dating hydrothermal-vein formation. Geochronology 3, 123–147, ~~https://doi.org/10.5194/gchron-3-123-2021,~~https://doi.org/10.5194/gchron-3-123-2021, 2021.

Peverelli, V., Berger, A., Mulch, A., Pettke, T., Piccoli, F., and Herwegh, M.: Epidote U–Pb geochronology and H isotope geochemistry trace pre-orogenic hydration of mid-crustal granitoids, GEOLOGY, ~~accepted.~~2022.

925 https://doi.org/10.1130/G50028.1

Pongrac, P., Jeřábek, P., Stünitz, H., Raimbourg, H., Heilbronner, R., Racek, M., Nègre, L.: Mechanical properties and recrystallization of quartz in presence of H2O: Combination of cracking, subgrain rotation and dissolution-precipitation processes. J. Struct. Geol. 160. https://doi.org/10.1016/j.jsg.2022.104630, 2022.

Putnis, A.: Mineral replacement reactions: from macroscopic observations to microscopic mechanisms. Mineral. Mag. 66, 689–708, ~~https://doi.org/10.1180/0026461026650056,~~https://doi.org/10.1180/0026461026650056, 2002.

Putnis, A.: Mineral replacement reactions. Rev. Mineral. Geochemistry 70, 87–124, ~~https://doi.org/10.2138/rmg.2009.70.3, 2009~~https://doi.org/10.2138/rmg.2009.70.3, 2009.

Putnis, A., Austrheim, H.: Fluid-induced processes: Metasomatism and metamorphism. Geofluids 10, 254–269. https://doi.org/10.1111/j.1468-8123.2010.00285.x, 2010.

Putnis, A., John, T.: Replacement processes in the earth's crust. Elements 6, 159–164. https://doi.org/10.2113/gselements.6.3.159, 2010.

Putnis, A., Putnis, C. V.: The mechanism of reequilibration of solids in the presence of a fluid phase. J. Solid State Chem. 180, 1783–1786, ~~https://doi.org/10.1016/j.jssc.2007.03.023,~~https://doi.org/10.1016/j.jssc.2007.03.023, 2007.

Ramseyer, K., Baumann, J., Matter, A., Mullis, J.: Cathodoluminescence Colours of α -Quartz . Mineral. Mag. 52, 669–677, https://doi.org/10.1180/minmag.1988.052.368.11, 1988.

Rehkämper, M., Mezger, K.: Investigation of matrix effects for Pb isotope ratio measurements by multiple collector ICP-MS: Verification and application of optimized analytical protocols. J. Anal. At. Spectrom. 15, 1451–1460, ~~https://doi.org/10.1039/b005262k,~~https://doi.org/10.1039/b005262k, 2000.

Ricchi, E., Bergemann, C.A., Gnos, E., Berger, A., Rubatto, D., Whitehouse, M.J.: Constraining deformation phases in the Aar Massif and the Gotthard Nappe (Switzerland) using Th-Pb crystallization ages of fissure monazite-(Ce). Lithos 342–343, 223–238, ~~https://doi.org/10.1016/j.lithos.2019.04.014,~~https://doi.org/10.1016/j.lithos.2019.04.014, 2019.

Rolland, Y., Cox, S.F., Corsini, M.: Constraining deformation stages in brittle-ductile shear zones from combined field mapping and 40Ar/39Ar dating: The structural evolution of the Grimsel Pass area (Aar Massif, Swiss Alps). J. Struct. Geol. ~~31, 1377–1394, https://doi.org/10.1016/j.jsg.2009.08.003,~~31, 1377–1394, https://doi.org/10.1016/j.jsg.2009.08.003, 2009.

Rossi, M. and Rolland, Y.: Stable isotope and Ar/Ar evidence of prolonged multiscale fluid flow during exhumation of orogenic crust: Example from the mont blanc and Aar Massifs (NW Alps), 33, 1681–1709, https://doi.org/10.1002/2013TC003438, 2014.

Ruiz, M., Schaltegger, U., Gaynor, S.P., Chiaradia, M., Abrecht, J., Gisler, C., Giovanoli, F., Wiederkehr, M.: Reassessing the intrusive tempo and magma genesis of the late Variscan Aar batholith : U-Pb geochronology, trace element and initial Hf isotope composition of zircon. Swiss J. Geosci. 1–24. https://doi.org/10.1186/s00015-022-00420-1, 2022.

Schaltegger, U., Krähenbühl, U.: Heavy rare-earth element enrichment in granites of the Aar Massif (Central Alps, Switzerland). Chem. Geol. ~~89, 49–63, https://doi.org/10.1016/0009-2541(90)90059-G,~~89, 49–63, https://doi.org/10.1016/0009-2541(90)90059-G, 1990.

38

Schaltegger, U., Corfu, F.: The age and source of late Hercynian magmatism in the central Alps: evidence from precise U-Pb ages and initial Hf isotopes. Contrib. to Mineral. Petrol. ~~111, 329–344, https://doi.org/10.1007/BF00311195,~~111, 329–344, https://doi.org/10.1007/BF00311195, 1992.

Schmidt, M.W., Poli, S.: Magmatic epidote. Rev. Mineral. Geochemistry 56, 399–430, ~~https://doi.org/10.2138/gsrmg.56.1.399,~~https://doi.org/10.2138/gsrmg.56.1.399, 2004.

Schneeberger, R., Kober, F., Lanyon, G.W., Mäder, U.K., Spillmann, T., Blechschmidt, I.: Grimsel Test Site: Revisiting the site-specific geoscientific knowledge, 2019.

Seydoux-~~guillaume~~Guillaume, A., Montel, J., Bingen, B., Bosse, V., Parseval, P. De, Paquette, J., Janots, E., and Wirth, R.: Low-temperature alteration of monazite : Fluid mediated coupled dissolution – precipitation , irradiation damage , and disturbance of the U – Pb and Th – Pb chronometers, Chem. Geol., 330–331, 140–158, https://doi.org/10.1016/j.chemgeo.2012.07.031, 2012.

Stipp, M., Stünitz, H., Heilbronner, R., & Schmid, S. M.: Dynamic recrystallization of quartz: correlation between natural and experimental conditions. Geological Society, London, Special Publications, 200(1), 171-190. https://doi.org/10.1144/GSL.SP.2001.200.01.11, 2002.

Stünitz, H., Fitzgerald, J.D.F.: Deformation of granitoids at low metamorphic grade. II: Granular flow in albite-rich mylonites. Tectonophysics 221, 299–324, ~~https://doi.org/10.1016/0040-1951(93)90164-F,~~https://doi.org/10.1016/0040-1951(93)90164-F, 1993.

Tartèse, R., Ruffet, G., Poujol, M., Boulvais, P., Ireland, T.R.: Simultaneous resetting of the muscovite K-Ar and monazite U-Pb geochronometers: A story of fluids. Terra Nov. ~~23, 390–398, https://doi.org/10.1111/j.1365-3121.2011.01024.x,~~23, 390–398, https://doi.org/10.1111/j.1365-3121.2011.01024.x, 2011.

Tera, F., Wasserburg, G.J.: U-Th-Pb systematics in three Apollo 14 basalts and the problem of initial Pb in lunar rocks. Earth Planet. Sci. Lett. 14, 281–304, https://doi.org/https://doi.org/10.1016/0012-821X(72)90128-8, 1972.

Trincal, V., Lanari, P., Buatier, M., Lacroix, B., Charpentier, D., Labaume, P., Muñoz, M.: Temperature micro-mapping in oscillatory-zoned chlorite: Application to study of a green-schist facies fault zone in the Pyrenean Axial Zone (Spain). Am. Mineral. 100, 2468–2483. https://doi.org/10.2138/am-2015-5217, 2015.

Tullis, J.: Deformation of granitic rocks: Experimental studies and natural examples, Rev. Mineral. Geochemistry, 51, 51–95, https://doi.org/10.2138/gsrmg.51.1.51, 2002.

Villa, I.M., Hanchar, J.M.: K-feldspar hygrochronology. Geochim. Cosmochim. Acta 101, 24–33, ~~https://doi.org/10.1016/j.gca.2012.09.047,~~https://doi.org/10.1016/j.gca.2012.09.047, 2013.

Wehrens, P., Berger, A., Peters, M., Spillmann, T., and Herwegh, M.: Deformation at the frictional-viscous transition: Evidence for cycles of fluid-assisted embrittlement and ductile deformation in the granitoid crust, Tectonophysics 693, 66–84, https://doi.org/10.1016/j.tecto.2016.10.022, 2016.

Wehrens, P., Baumberger, R., Berger, A., Herwegh, M.: How is strain localized in a meta-granitoid, mid-crustal basement section? Spatial distribution of deformation in the central Aar massif (Switzerland). J. Struct. Geol. ~~94, 47–67, https://doi.org/10.1016/j.jsg.2016.11.004,~~94, 47–67, https://doi.org/10.1016/j.jsg.2016.11.004, 2017.

Weis, D., Kieffer, B., Maerschalk, C., Barling, J., De Jong, J., Williams, G.A., Hanano, D., Pretorius, W., Mattielli, N., Scoates, J.S., Goolaerts, A., Friedman, R.M., Mahoney, J.B.: High-precision isotopic characterization of USGS reference materials by TIMS and MC-ICP-MS. Geochemistry, Geophys. ~~Geosystems 7, https://doi.org/10.1029/2006GC001283,~~Geosystems 7, https://doi.org/10.1029/2006GC001283, 2006.

Williams, I. S.: U-Th-Pb geochronology by ion microprobe, Rev. Econ. Geol., 7, 1–35, 1998.

Williams, M.L., Jercinovic, M.J., Harlov, D.E., Budzyń, B., Hetherington, C.J.: Resetting monazite ages during fluid-related alteration. Chem. Geol. 283, 218–225, https://doi.org/10.1016/j.chemgeo.2011.01.019, 2011.

Wintsch, R.P., Yeh, M.W.: Oscillating brittle and viscous behavior through the earthquake cycle in the Red River Shear Zone: Monitoring flips between reaction and textural softening and hardening. Tectonophysics 587, 46–62, ~~https://doi.org/10.1016/j.tecto.2012.09.019,~~https://doi.org/10.1016/j.tecto.2012.09.019, 2013.